REPORT CDOT-2022-05 June 2022

Linking Measurement from a Differential Emissivity Imaging Disdrometer (DEID) to Storm-Snow Instabilities

APPLIED RESEARCH & INNOVATION BRANCH

Eric Pardyjak, Travis Morrison, Trent Meisenheimer, Dhiraj Singh, Spencer Donovan, Timothy Garrett

COLORADO Department of Transportation

TECHNICAL REPORT DOCUMENTATION PAGE

1. Report No. CDOT-2022-05	**2. Government Accession No.**	**3. Recipient's Catalog No.**
4. Title and Subtitle Linking Measurements from a Differential Emissivity Imaging Disdrometer (DEID) to Storm-Snow Instabilities		**5. Report Date** June 2022 **6. Performing Organization Code**
7. Author(s) Eric Pardyjak, PhD; Travis Morrison, PhD; Trent Meisenheimer; Dhiraj Singh, PhD; Spencer Donovan; Timothy Garrett, PhD		**8. Performing Organization Report No.**
9. Performing Organization Name and Address University of Utah 201 S. Presidents Circle Salt Lake City, UT 84112		**10. Work Unit No.** **11. Contract or Grant No.** **Study No: 5337-20-09**
12. Sponsoring Agency Name and Address Colorado Department of Transportation - Research 2829 W. Howard Place Denver, CO 80204		**13. Type of Report and Period Covered** Final **14. Sponsoring Agency Code**

15. Supplementary Notes
Performed in cooperation with the Federal Highway Administration.

16. Abstract
This report describes a collaborative study conducted by the University of Utah Environmental Fluid Dynamics (EFD) Lab in collaboration with Particle Flux Analytics, Inc., Alta Ski Patrol and the Utah Department of Transportation (UDOT). The objectives of the project were to: (1) field test the Differential Emissivity Imaging Disdrometer (DEID) in Little Cottonwood Canyon and (2) link the results from the DEID to snow-stability metrics. Ultimately, this project aims to provide more information to help DOT forecasters make better decisions in a timely manner. The DEID is a thermal and optical instrument designed to measure the mass, size, density, and type, as well as visibility. The DEID can make these measurements at an unprecedented sampling rate (approximately once every second). DEID observations of snow accumulation, snow water equivalent (SWE) accumulation and snow density from seventeen storms taken at the mid-Collins Snow-Study Plot at Alta Ski Area during winter 2020-2021 showed excellent agreement with manual measurements with R^2 values of 0.994, 0.983 and 0.875, respectively. Three methods were investigated to link DEID measurements to new-snow storm instabilities. The most promising of these methods is a stability-index model (also known as the SNOw Slope Stability model, SNOSS) that takes advantage of the DEID's ability to measure SWE and snow density in real time. Four new-snow stability models were run and evaluated with data collected from the DEID. The models show good agreement with tilt-board tests, infrasound data and visual observations of avalanches. Results show that over the 11 storms analyzed, the minimum stability index predicts the number of observed avalanches (naturals plus unknown) in the central Wasatch with an R^2 value of 0.40. Finally, the report discusses several challenges associated with the measurements and recommended future work.

17. Key Words Avalanche, Snow water equivalent, Snow density, Storm-snow instability, Remote measurements	**18. Distribution Statement** This document is available on CDOT's website https://www.codot.gov/programs/research

19. Security Classif. (of this report) Unclassified	**20. Security Classif. (of this page)** Unclassified	**21. No. of Pages**	**22. Price**

The contents of this report reflect the views of the author(s), who is(are) responsible for the facts and accuracy of the data presented herein. The contents do not necessarily reflect the official views of the Colorado Department of Transportation or the Federal Highway Administration. This report does not constitute a standard, specification, or regulation.

ACKNOWLEDGMENTS

We wish to thank Steven Clark and Jamie Yount, our DOT Champions, for their guidance and support during the project. We thank Dave Richards and the Alta Ski Patrol for their help and contributions, which were critical to facilitating the field validation study at Alta Ski Area. We thank the Utah Avalanche Center from providing access to backcountry observations and data. We are also thankful to Mark Saurer for the help working with UDOT infrasound data. We thank Karl Birkeland and Ethan Greene for their help in the proposal phase of the project. We thank Allan Reaburn and his colleagues at Particle Flux Analytics for their key contributions in the development of DEID. The DEID is protected and commercially available through Particle Flux Analytics, Inc. Co-author Tim J. Garrett is a co-owner of Particle Flux Analytics. In addition to the support provided by TARP, this research was accomplished via support from the U.S. National Science Foundation grant number PDM-1841870.

SUMMARY

This report describes a collaborative study conducted by the University of Utah Environmental Fluid Dynamics (EFD) Lab in collaboration with Particle Flux Analytics, Inc., Alta Ski Patrol and the Utah Department of Transportation (UDOT). The objectives of the project were to: (1) field test the Differential Emissivity Imaging Disdrometer (DEID) in Little Cottonwood Canyon and (2) link the results from the DEID to snow-stability metrics. Ultimately, this project aims to provide more information to help DOT forecasters make better decisions in a timely manner. The DEID is a thermal and optical instrument designed to measure the mass, size, density, and type, as well as visibility. The DEID can make these measurements at an unprecedented sampling rate (approximately once every second).

DEID observations of snow accumulation, snow water equivalent (SWE) accumulation and snow density from seventeen storms taken at the mid-Collins Snow-Study Plot at Alta Ski Area during winter 2020-2021 showed excellent agreement with manual measurements with R^2 values of 0.994, 0.983 and 0.875, respectively. Three methods were investigated to link DEID measurements to new-snow storm instabilities. The most promising of these methods is a stability-index model (also known as the SNOw Slope Stability model, SNOSS) that takes advantage of the DEID's ability to measure SWE and snow density in real time. Four new-snow stability models were run and evaluated with data collected from the DEID. The models show good agreement with tilt-board tests, infrasound data and visual observations of avalanches. Final results show that over the 11 storms analyzed, the minimum stability index predicts the number of observed avalanches (naturals plus unknown) in the central Wasatch with an R^2 value of 0.40. Finally, the report discusses several challenges associated with the measurements and recommended future work.

CHAPTER 1

INTRODUCTION

1.1 CONTEXT

Results and findings from the TARP-funded instrument development project (Study No: 5337-20-09) are presented. The instrument that was developed and validated is the Differential Emissivity Imaging Disdrdometer (DEID). The DEID is a novel hotplate disdrometer, which captures real-time measurements of snow density, snow water equivalent (SWE), and precipitation intensity (PI) on a particle-by-particle basis at a high temporal resolution (Singh et al., 2021). In addition to these standard measured hydrometeor variables, the DEID has been shown to also characterize snowflake shape and complexity, through two new variables: shape density index or SDI and $Complexity$. Together, we have also investigated how these variables can be used to model and forecast new-snow instabilities using data collected solely from the DEID.

Observations collected during winter 2020-2021 and 2021-222 and results from a new-snow instability model are evaluated and validated against the measurements routinely available in Little Cottonwood Canyon, Utah. Data from unique resources such as Utah Department of Transportation's (UDOT's) Wyssen Ida Infrasound Detection System (Vyas, 2009; Stephanie et al., 2020), a high-density network of standard meteorological stations, and physical observations from snow professionals and recreationalists managed by the Utah Avalanche Center (UAC) are used to demonstrate the power and accuracy of the DEID and the resulting new-snow instability model.

1.2 MOTIVATION

New-snow or storm-snow avalanches in alpine terrain are the cause of significant hazards to roadways, motorists, maintenance personal, and infrastructure, closing mountain corridors throughout many areas including Europe, North America, and New Zealand. Forecasting these avalanches with a high degree of spatial and temporal accuracy (sub 1 kilometer and 1 hour) has plagued avalanche forecasters and mitigation operators for decades and leads to large economic impacts. While the impact of avalanches on human life are likely the most significant consequence, damages to infrastructure and road closures as a result of avalanches can also cause major problems. For example, SR-210 along Little Cottonwood Canyon (LCC) in Utah, is a high-traffic mountain highway where avalanche mitigation results in significant downtime. As a result of storms and mitigation work, LCC closes, on average, 10.4 times for a total 57.3 hours per year. However, on snow years that significantly exceed average accumulations, those numbers can more than double. The

cost of such closures has been estimated at over $2.5 million per day, or $106,000 per hour in 2019 dollars (Nalli, 2019).

Current techniques for measuring valuable forecasting variables for current condition assessment and weather-forecasting model assimilation rely on accurate observations of snow density, SWE, and PI. These variables are currently measured using either a weighing bucket or with manual measurements at ski areas and managed weather stations. The measurements are relatively costly and often result in poor temporal resolution, leading to a set of retroactive data, rather than a real-time set of observations. Furthermore, assessment of snowflake structure and the strength of snow layers can currently only take place after loading has occurred through snow-pit evaluation tests (e.g., ETCs, PSTs, etc.), which is often long after the avalanche danger has created impending threats to the public.

Hence, there is a critical need for real-time, observation-based tools (both hardware and software) that account for the ubiquitous spatial variability in atmospheric and snow-related variables found in mountainous terrain. There is a need to have spatially explicit data with accompanying warning notices and alerts associated with rapidly changing conditions in mountains that are easily available to forecasters and DOT operators. This project attempts to address these issues through the experiments and models described in the following sections.

1.3 GOALS

Task 1: Evaluate the DEID measurements - To accomplish this task, we deployed the DEID for a complete winter season (2020-2021) at the Alta-Collins snow-study plot. We evaluated the DEID's ability to quantify snow density, snow water equivalent (SWE) and total snowfall (HST).

Task 2: Understand the implications of real-time measurements of snow density, SWE, and snowflake characteristics on storm-snow stability - Three main approaches were pursued for this task: (i) we investigated various DEID parameters and linked them to stability indices and/or avalanches, (ii) we attempted to link new-storm instability to DEID data with systematic *tilt-board tests*, and (iii) we adapted and developed a stability model based on the ratio of new-storm overburden to snow strength.

CHAPTER 2

METHODS

We first describe the DEID's basic measurement principles and then present the methodology for computing key variables that are reported by the DEID. Next, we describe a new-snow instability model that takes advantage of the DEID's unique measurements (SWE rate, density, SDI, and $Complexity$). Finally, we describe the infrastructure and field experiment setup used to evaluate the DEID at the Alta Collins study plot.

2.1 DEID METHODOLOGY

A complete description of the the DEID is presented in Singh et al. (2021) with additional details given in Rees et al. (2021). Here, we present a concise summary. The DEID consists of an infrared camera pointed at a hotplate that has low emissivity. To quantify a hydrometeor's size/area on the hotplate, the DEID makes use of the fact that the thermal emissivities of water ($\varepsilon > 0.95$) and aluminum ($\varepsilon < 0.1$) are very different. As a result of these different emissivities, objects that have the same actual temperature yield different radiative temperatures when visualized with a thermal camera (see Fig. 2.3). An energy balance is applied across each individual hydrometeor that lands on the DEID to estimate the mass of individual hydrometeors. The actual temperature of the plate is measured using high-emissivity ($\varepsilon \approx 0.95$) polyimide tape, which is applied to one of the corners of the heated plate. A thermal camera is used to measure surface temperatures at 15 fps with a resolution 531 pixels $\times$ 362 pixels, resulting in a spatial resolution of about 0.2 mm/pixel.

The measurement of the mass of individual hydrometeors is based on calculations that use the thermal images of the hotplate (gray-scale images), which provide the area of hydrometeors, the temperature difference between hydrometeor on the plate and the hotplate, as well as the complete evaporation time. Individual hydrometeor mass is determined using the DEID by assuming that the heat gained by a hydrometeor is equivalent to the heat lost by the hotplate during the complete evaporation. The mass of individual hydrometeors is estimated using Eq. 2.1, which is based on energy conservation across water droplet.

$$m = \frac{1}{(c\Delta T + L_{eqv})} \int_0^{\Delta t} (k/d)_{eff} A(t)(T_p(t) - T_w(t))dt. \tag{2.1}$$

For a snowflake, the snow water equivalent may be immediately calculated as, $SWE = (c_1 \Delta m)(A_{hp}\rho_{H_2o})$; c_1 is conversion factor from meters to millimeters (i.e. $c_1 = 10^3$ mm m^{-1}), Δm (kg) is the total hydrometeor

mass that falls on the hotplate in a given time, A_{hp} (m^2) is a rectangular sampling area on the hotplate and SWE is given in mm of water. In Eq. 2.1, c is the specific heat capacity of water, L_v is the latent heat of vaporization of water, T_p is the hotplate surface temperature, T_w is the temperature of the water droplet, and ΔT is the temperature difference between the initial and final temperature of a water droplet on the hotplate. In addition, L_{eqv} = L_v is applied for liquid hydrometeors and L_{eqv} = $L_v + L_f$ for solid hydometeors, where L_f is latent heat of fusion for water. dt (approximated as Δt) is the time required to evaporate the water droplet, and $(k/d)_{eff}$ is an empirical coefficient that has been determined to be 7.006×10^3 W m^{-2} K^{-1}.

The SWE accumulation rate ($S\dot{W}E$) can also be estimated using the DEID. To compute the SWE rate the total mass of water deposited onto the hotplate in each frame, therefore the SWE rate for a given time interval may be written as,

$$S\dot{W}E = c_2 \frac{\Delta m \cdot fps}{\rho_w A_{hp}}, \tag{2.2}$$

where c_2 is a conversion factor from m s^{-1} to mm hr^{-1} (3.6×10^6 mm h^{-1} m^{-1} s), fps is the image sampling rate in frames per second, Δm (kg) is the total hydrometeor mass that falls on the hotplate in each recorded frame that is estimated using Eq. 2.1, ρ_w (kg m^{-3}) is the bulk density of water and A_{hp} (m^2) is a rectangular sampling area on the hotplate that captures all hydrometeors.

In addition to this frame-by-frame method, SWE and $S\dot{W}E$ can be estimated using a particle-by-particle method. In this case, Δm in Eq. 2.2 is the total hydrometeor mass that falls on the hotplate over a given time interval Δt in Eq. 2.2, which is the sum of all individual hydrometeors that have completed the normal cycle of evaporation.

The density of individual snowflakes is estimated by $\rho_s = m/V$, where m (kg) and V (m^{-3}) are the mass and volume of an individual snowflake, respectively. The volume V can be estimated by assuming a spherical particle of equivalent circular diameter D_{eff} such that $V = (\pi/6)D_{eff}^3$. The probability of non-spherical snow particle precipitation is high, leading to misguiding the density estimation. Therefore, we developed a method to estimate density based on heat flux and independent of shape.

The heat flux from the hotplate into the single snowflake as

$$E = \frac{H}{A_e \Delta t} \tag{2.3}$$

Where A_e is the maximum observed area of the snowflake on the hotplate before it evaporates. H = mL_{eqv} is the total energy required to melt and evaporate the snowflake from the hotplate. And Δt is evaporation time. From observations, we find that for a given area and evaporation time, multiple values of E can be obtained for a given value of snowflake mass due to the varying amounts of liquid water, implying that the snowflake density is correlated with the heat flux. Thus, we hypothesize that the heat flux method can be used to compute the density of different types of snowflakes through comparison to a reference as follows

$$\rho_s = \rho_0 \frac{E}{E_0}. \tag{2.4}$$

Values for ρ_0 and E_0 were determined from field measurements and validated in laboratory experiments. The average density ($\overline{\rho}_s$) prior to settling over a given period can be calculated from DEID data using the ratio of the total mass to total volume in a given time interval, namely

$$\overline{\rho}_s = \frac{\sum_{i=1}^{N} m_i}{\sum_{i=1}^{N} m_i/\rho_{s,i}}, \tag{2.5}$$

where m_i (kg) is the mass of i^{th} snowflake, $\rho_{s,i}$ (kg m^{-3}) the density of the i^{th} snowflake and N is the total number of snowflakes on the plate during the given time frame. From the average density of the snowflakes in each frame, the snow precipitation rate or precipitation intensity is,

$$PI_{snow} = c_2 \frac{\Delta m \cdot fps}{\overline{\rho}_s A_{hp}}. \tag{2.6}$$

Total snow accumulation, HS (mm), is then computed by multiplying the precipitation rate by the time interval between samples ($1/fps$) and then summed over the period of interest (i.e., storm or hourly).

Visibility can be estimated using the Koschmieder relation (Gultepe and Milbrandt, 2010; Rasmussen et al., 1999) , which is given in details in (Singh et al., 2021).

2.2 INSTABILITY MODEL

Instability in the evolving fresh snowpack can be determined with DEID measurements using a simple physics-based model. In this case, we adapt the SNOw Slope Stability model (SNOSS) (Hayes et al., 2004). The stability index used here is defined as the ratio of the strength of a buried layer to the shear stress imposed by the overburden stress from the snowpack above, such that the snowpack becomes unstable when the stability index approaches and falls below a value of unity (Conway and Wilbour, 1999; Hayes et al., 2004; Havens et al., 2012). In order to evaluate the stability index, the following parameters are required: the shear strength of the buried layers, which depend on crystal shape, type, and density of grain form, and the imposed shear stress from the weight of the overburden and slope angle of the terrain of interest. Following Jamieson and Johnston (2001), the shear strength (in kPa) of a buried layer ($\alpha(z,t)$) at a depth z and at time t after the snow begins to accumulate may be written as,

$$\alpha(z,t) = \lambda \left(\frac{\rho_s}{\rho_i} \right)^{\beta}, \tag{2.7}$$

where $\rho_s(z,t)$ is the density of a given snowpack layer, ρ_i is density of ice (ρ_i = 917 kg m^{-3}) and λ and β are empirical constants that depend on the ice grain form. This formulation is related to Young's modulus of ice, which provides a power-law behavior that is supported through manual observations (Perla, Beck and Cheng, 1982; Jamieson, 1995). Typically, λ and β are derived from fitting experimental measurements of shear strength of precipitation particles with a strain gauge. In the present work, we use two sets of precipitation-particle values. The first are the precipitation particle values recommended by Jamieson and Johnston (2001): $\lambda = 5.32$ kPa and $\beta = 1.35$, and the second are the DEID-derived values that are explained below. Results from both methods are computed with a constant density in time and with a densification model, providing a total of four shear-strength models. Using the four models, supplies a range of forecasted stabilities and increases the predictive accuracy through ensemble averaging (i.e., statistical forecasting). A summary of these models are supplied in Table 2.1.

Over the course of a storm, each layer of the storm snow will increase in density through both metamorphic and stress from the gravitational component of the overburden weight ($\sigma_{zz}(t) = g \int \dot{SWE} \cos^2\theta \, dt$). For simplicity, the metamorphic stress ($\sigma_m(t)$) is assumed to be a constant (= 75 Pa) and is added to the overburden stress (Conway and Wilbour, 1999). This value assumes that the near-surface (5–10 cm) densification of the storm snow is dominated by the metamorphic processes, and is driven by the gravitational component for layers that are deeper than 5 to 10 cm from the surface. By assuming a viscous densification law for dry storm

Model	λ (kPa)	β	Description
Jamieson 2001, no densification	5.32	1.35	Constant coefficients of strength
Jamieson 2001, with densification	5.32	1.35	Constant coefficients of strength
SDI & $Complexity$, no densification	SDI	$Complexity$	Coefficients are a function of snowflake structure
SDI & $Complexity$, with densification	SDI	$Complexity$	Coefficients are a function of snowflake structure
Ensemble	—	—	Average of all model outputs

TABLE 2.1
A summary of the four models evaluated during the study as well as the ensemble, which is the average of the four other models in the table.

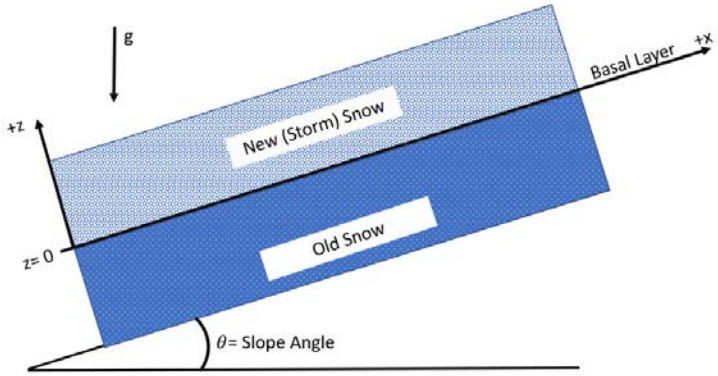

FIGURE 2.1
Coordinate convention reference for a new-storm slab on a slope with an inclination angle θ

snow, the density of the snow ($\rho_z(t)$) can be expressed at each layer and point in time as follows,

$$\frac{1}{\rho_z(t)}\frac{d\rho_z}{dt} = \frac{1}{\eta_{zz}}[\sigma_m(t) + \sigma_{zz}(t)]. \tag{2.8}$$

Here, $\eta_{zz}(t)$ represents the compactive viscosity for dry snow, which was experimentally determined from Kojima (1967) and modified with an Arrhenius type temperature term by Conway and Wilbour (1999),

$$\eta_{zz}(t) = B_1 e^{B_2\left(\frac{\rho_z(t)}{\rho_i}\right)} e^{E/RT_z}. \tag{2.9}$$

The following constants, B_1 = 6.5×10^{-7} Pa s, $B_2 = 19.3$, the activation energy E = 67.3 kJ^{-1} mol^{-1}, the ideal gas constant for air R = 0.0083 kJ^{-1} mol^{-1} K^{-1}, and the layer temperature T_z = 273 K were utilized in the calculation of η_{zz}. Equations 2.8 and 2.9 were then discretized and solved with Euler's method and an initial density profile provided by the DEID. The coupled model with the DEID inputs yields high-resolution maps of snow-layer density as a function of time.

The overburden stress (W), which considers both gravitational and shear forces on terrain with a slope angle (θ), is expressed as

$$W(z,t) = g\int_0^t S\dot{W}E(t)\sin(\theta)\cos(\theta)dt, \tag{2.10}$$

where $S\dot{W}E(t)$ is SWE rate at time t. Hence, the stability index (SI) is the ratio of the shear strength (Eq.

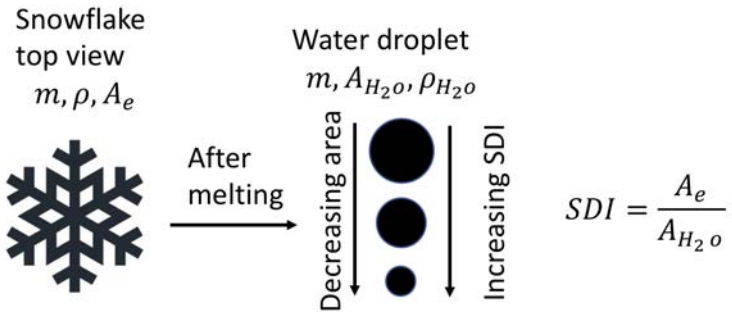

FIGURE 2.2
Schematic of the calculation of SDI for each snowflake. A_e is the area of snowflake, A_{H_20} is the area of spherical water droplet after melting. The down arrow indicates decreasing water droplet area after melting (a smaller area for less dense snowflakes). As a result, the less dense the snowflake, the larger the SDI.

2.7) to the overburden force of the overlaying snow (Eq. 2.10),

$$SI(z,t) = \frac{\alpha(z,t)}{W(z,t)}. \tag{2.11}$$

For values of SI $\gg 1$, the snowpack should be stable, while for SI ≤ 1, the snowpack should exhibit instability. The DEID provides real-time values of ρ_s and $S\dot{W}E(t)$ so that the stability index can, for the first time, be calculated in real-time during a storm to forecast time to failure within new-snow layers.

2.2.1 NEW GOVERNING PARAMETERS: SDI AND COMPLEXITY

This section describes the development of two new parameters, the hydrometeor shape density index (SDI) and $Complexity$. These variables were derived to provide easily obtainable parameters that could be measured by the DEID which may identify precipitation types. SDI is defined as the ratio of the snowflake area A_e to the melted area of a spherical water droplet A_{H_20} with the same mass (Eq. 2.12),

$$SDI = \frac{A_e}{A_{H_20}}. \tag{2.12}$$

The melted area of a spherical droplet of the same mass is can be expressed (after some algebra) as,

$$A_{H_20} = C_{SDI}(\frac{m}{\rho_{H_20}})^{2/3}. \tag{2.13}$$

Here, $C_{SDI} = 1.21$ is a geometric constant, m is the mass of the snowflake, and ρ_{H_20} is the density of water taken to be 1000 kg m^{-3}. To gain a better understanding a schematic of SDI is supplied in Figure 2.2. The minimum value of SDI is near unity for spherical snow particles, which has density close to water.

The particle $Complexity$ is defined as the ratio of the area of the smallest ellipse altogether containing the particle cross-section to the actual cross-sectional area A_e of the hydrometeor measured on the hotplate and is illustrated in Figure 2.3. The areas used to calculate each individual particle's $Complexity$ are determined using Matlab's image processing toolbox, Regionprops (MajorAxisLength and MinorAxisLength).

$$Complexity = \frac{\pi ab}{A_e}. \tag{2.14}$$

where, a and b are the major and minor axis length of ellipse that fit over the snowflake. The minimum value of complexity is unity for a circular snow particle.

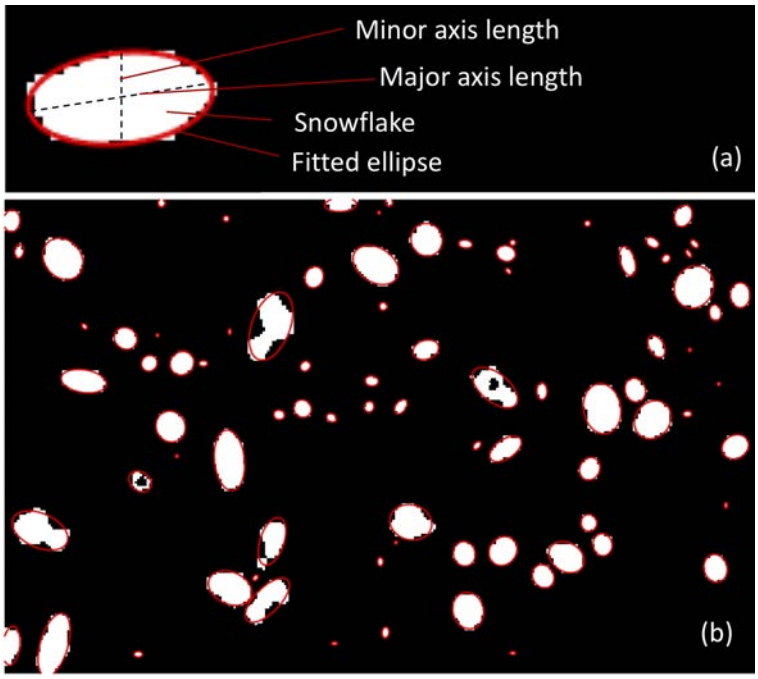

FIGURE 2.3
(a) Illustration of the major-axis length and minor-axis length of the ellipse fit over a snowflake; (b) a black and white image showing melting snowflakes on the hotplate of the DEID as seen by the thermal camera during a snow event. Using Matlab's image-processing toolbox, the DEID tracks individual hydrometeors as they impact the hotplate, melt, and evaporate. Through tracking this process and measuring the snowflake area, as well as the area of the ellipsoid containing the snowflake, the SDI and $Complexity$ are derived.

2.2.2 IDENTIFICATION OF SNOWFLAKE HABIT USING SDI AND COMPLEXITY

A combined laser-SLR camera system and the DEID can be used together to determine snow-crystal type. A 7 cm thick laser sheet for illuminating snowflakes was generated by merging three green 10-W lasers (520 nm wavelength) and then focusing the laser into a plane with spherical lenses. High-resolution images of snowflakes were acquired using a Nikon D850 SLR camera with a Nikon AF-S VR Micro - Nikkor 105 mm f/2.8 G IF-ED lens. The laser sheet was oriented such that falling snowflakes are photographed once they enter the plane. The bottom of the laser sheet was situated about 2 cm above the hotplate of the DEID, such that falling snowflakes captured by the SLR camera can be directly correlated with DEID measurements. The type of snowflake crystal was categorized based on the international classification for seasonal snow on the ground (Fierz et al., 2009). Due to the limitation of 2-D snowflake images, we categorized six habits of the snowflake (Praz, Roulet and Berne, 2017), planar crystal (combining stellars and plates), graupel (combining hail and graupel), columnar crystal, irregular crystal, aggregate and small particles.

Figure 2.4 presents six different hydrometeor types along with five snowflake examples of each crystal type. Our single camera classification technique has been successful because individual snowflakes rotate as they fall in the laser plane, providing snapshots from multiple angles of each hydrometeor (unlike other systems that utilize multiple cameras, for example the Multi-Angle Snowflake Camera – MASC (Garrett et al., 2012). The selection of crystal type was based on all images of individual snowflakes captured by the SLR to represent one type of crystal. After landing, the SDI and complexity of each type of crystal were calculated using the measured mass and area of an individual snowflake from the DEID. For each snowflake habit, 21

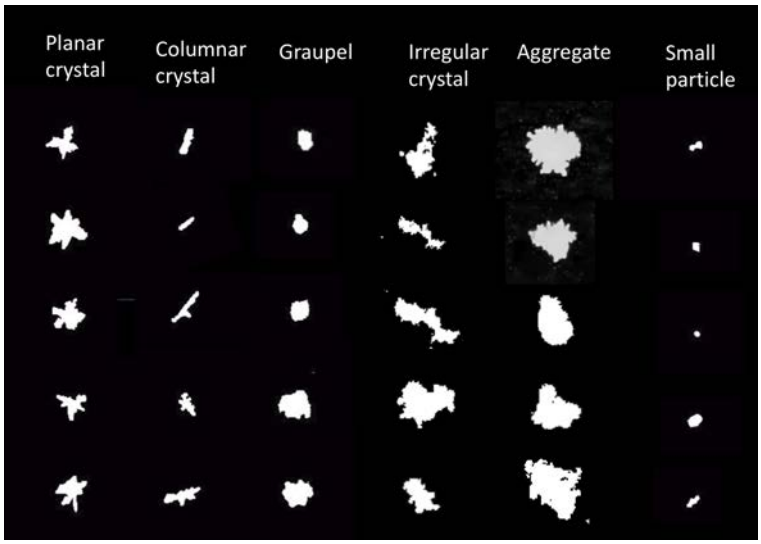

FIGURE 2.4
Various snowflake images obtained from the SLR camera taken at the Alta-Collins snow-study plot. Black and white images of six types of snowflakes are illustrated. Each type consists of five samples.

samples were taken to correlate with the corresponding SDI and $Complexity$. This process was done by visually inspecting individual snowflakes. A summary of the snowflake habit as a function of the SDI and $Complexity$ is provided in Table 2.2.

TABLE 2.2
Preliminary estimates of the relationship between SDI, complexity and snowflake crystal subclass.

Crystal Subclass	**SDI - λ (kPa)**	**Complexity - β**
Planar crystals	6.12 - 14.89	1.21 - 1.53
Columnar crystals	13.65 - 19.89	1.41 - 1.59
Graupel	3.21 - 6.53	1.10 - 1.18
Irregular Crystals	16.23 - 21.83	1.31 - 1.49
Aggregates	18.75 - 28.30	1.18 - 1.34
Small particles	2.11 - 8.96	1.00 - 1.21

2.2.3 RELATING SDI AND COMPLEXITY TO SHEAR STRENGTH

Extensive research has been performed on the shear strength of the buried old snow layers crystal structure as a function of density and grain type (Schweizer, Bellaire et al., 2006). Casson, Stoelinga and Locatelli (2008) explored the importance of new snowflake habit on the shear strength relationship with data collected from Snoqualmie Pass. This work revealed that simple shear strength parameterizations for precipitation particles may over simplify the intricacies of the strength of each snowflake habit. For example, we should anticipate that light dendrites, which have a low density exhibit a lower shear strength, and needles, which are slightly higher density, have higher strength. Based on our work linking SDI and $Complexity$ to snowflake habit, we hypothesize that the coefficients of strength can be substituted with these variables such that $\lambda = SDI$ (with units of kPa) and $\beta = Complexity$ (unitless).

In order to begin to test this hypothesis, we calculate the mean of SDI and $Complexity$ for each 5-mm layer and calculate the shear strength from Equation 2.7. Here, we acknowledge each layer (5 mm) of snowpack consists of several numbers and types of crystals, and may not linearly average (which we assume to be the case). The calculated shear strengths is then compared against the standard fixed coefficient models from Jamieson and Johnston (2001), Conway and Wilbour (1999), Brun and Rey (1987), and Perla, Beck and Cheng (1982) (Figure 2.5). We find fair agreement between the newly propose SDI and $Complexity$ model and the accepted models; hence, we further explore the utility of SDI and $Complexity$ in the text that follows.

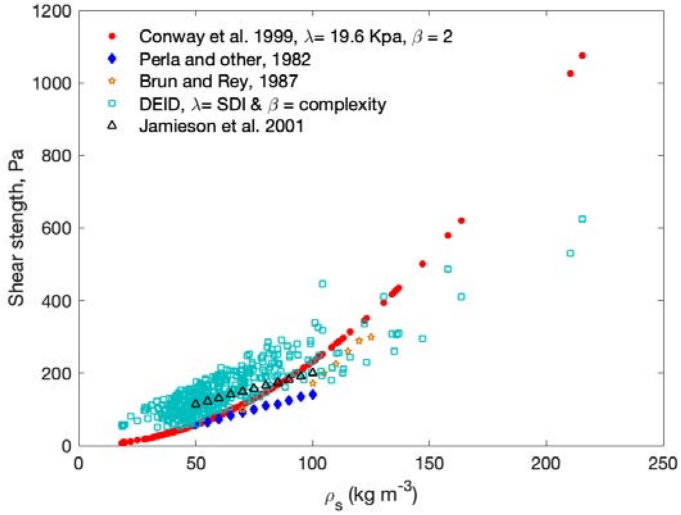

FIGURE 2.5
Shear strength of snow layers (each 5 mm thick) as a function of snow density using Eq. 2.7, where Λ and β are SDI (in kPa) and $Complexity$ (unitless), respectively and are compared with previously reported shear strength for weak layers by Conway and Wilbour (1999) – red solid circles, Perla, Beck and Cheng (1982) – blue solid diamonds Brun and Rey (1987) – hollow stars and Jamieson and Johnston (2001) – black hollow triangles.

2.3 EXPERIMENTAL SITE AND SETUP

Experimental data collection occurred during the 2020-2021 and 2022 winter seasons in Upper Little Cottonwood Canyon, Utah, USA at the Alta Ski Area mid-Collins Snow Study Plot (40.5763° N, 111.6383° W, 2920 m above sea level). The mid-Collins Snow Study Plot is 24 m wide from east to west and 45 m from north to south. The plot is roped off and is off limits to resort guests, such that the snow surface remains protected and undisturbed. The study plot is surrounded by trees and open to the sky, providing an ideal setting for measuring snow fall. At a larger scale, the study plot sits in the Collins drainage, surrounded by Mt. Baldy (elevation of 3374 m) to the southwest, with extending ridgelines to the North that decrease in elevation to SR210. For further details, see Figure 2.6a, which provides a topographic map of the area around the study site (red star).

Figure 2.6b presents the DEID and supporting instrumentation. The apparatus was placed on a permanent 6 m tall 10.16 cm $\times$ 10.16 cm square steel box-section tower with two pulleys/winches fixed with a concrete base, which allowed the experimental apparatus to raise and lower as snow accumulated throughout the

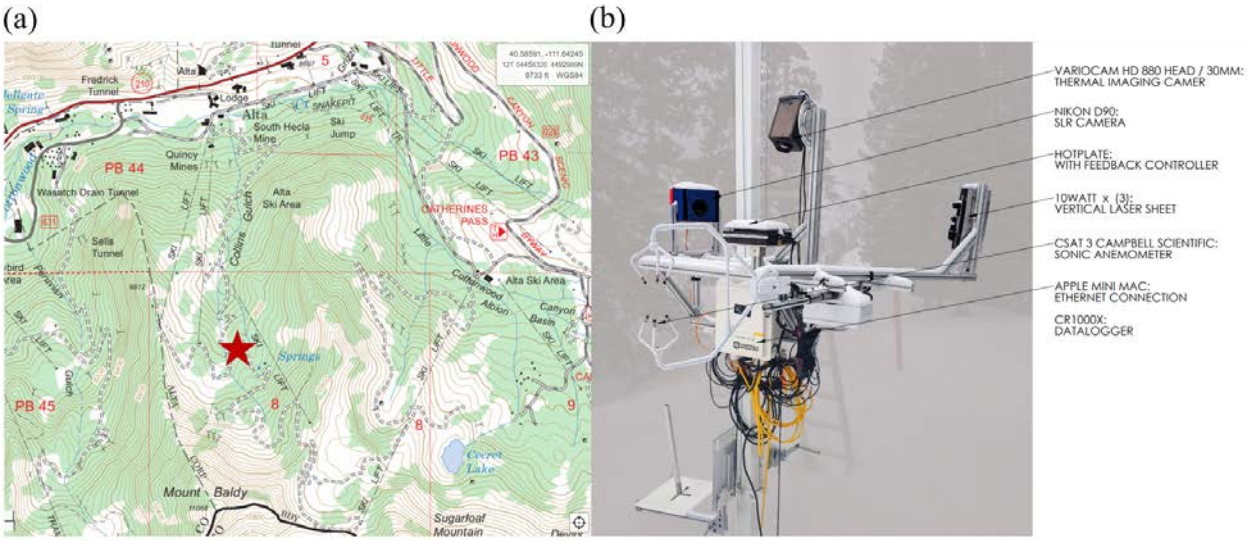

FIGURE 2.6
(a) Topographic map showing the location of the Alta Ski Area mid-Collins Snow Study plot marked with a star and (b) photograph of the DEID experimental setup during Winter 2020-2021.

winter. A mounting system constructed from 80/20 T-slot aluminum building system (Columbia City, Indiana, USA) was fixed to the pulley/winch system on the tower. The DEID was attached to the mounting system, suspended in the air and off the snow surface, allowing for direct snowfall onto the hot plate. The DEID's individual components were all carefully connected to the 80/20 aluminum frame. The DEID consists of a hotplate with a feedback controller and a thermal camera pointing at the hotplate. The hotplate is a Systems and Technology International, Inc. HP-606-P. The custom hotplate has a heated area of 0.1524 m $\times$ 0.1524 m and a thickness of 0.0508 m (used area of hotplate by thermal camera is 6.5 cm $\times$ 8.7 cm) and is powered by a 120 V, 5-Amp supply with a digital proportional integral derivative (PID) feedback control mechanism to control the plate temperature. The top plate surface is composed of 6061 180 aluminum alloy with a thermal conductivity, k = 205 W m^{1}K^1, which was roughened using 2000 grit sandpaper in a linear motion across the plate yielding long straight grooves. To maintain strong thermal contact, the aluminum plate was fixed to the top of the heater with thermal paste. On the top of the aluminum plate, a piece of Kapton® tape with high total hemispherical emissivity (ε =0.95) is affixed to the top plate to measure the actual surface temperature using the thermal camera. The maximum operating temperature of hotplate for Alta field experiments is 106 °C, such that when a hydrometeor lands on the surface it rapidly evaporates. The thermal camera used for all experiments is an uncooled microbolometer Infratec Vario HD 700 thermal camera with 432 × 288 pixel resolution, sampling at a rate of 15 Hz. Note that the thermal camera only measures the correct temperature of the surface when the emissivity of the plate surface is high (i.e, when a hydrometeor lands on the surface). Otherwise the low emissivity of the plate surface renders the background brightness temperature small.

In addition to the system's main components, Alta Ski Area provided a wired ethernet connection that facilitated the rapid transfer of images from the PC located at the study plot to a workstation at the University of Utah where post processing of the images occurs. This is extremely important as 1 hr of images is approximately 1.2 GB of data. During winter 2020-2021, images were downloaded in batches during or after the storm and processed with a Matlab script described in Singh et al. (2021).

To compliment this deployment, a wide variety of snow-measuring instruments and manual observation boards

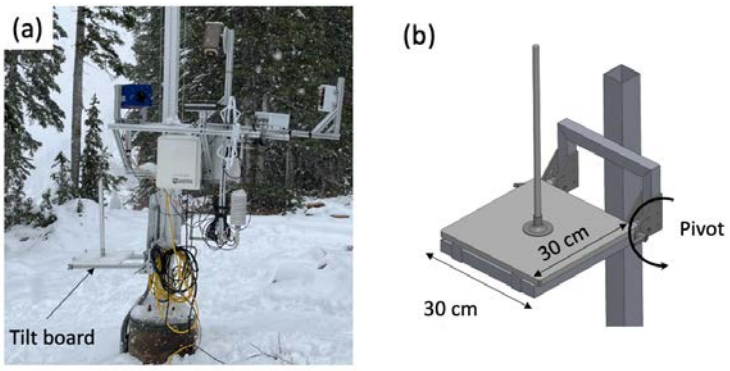

FIGURE 2.7
(a) Tilt board deployed in the field (b) Solidworks rendering of the tilt board.

are deployed and maintained by the Alta Avalanche Office at the mid-Collins study plot. The observation boards used include three main manual snow measuring boards that are used for measuring the amount of snowfall at different time intervals during a storm, specifically at 12 hr, 24 hr, and at the end of the storm duration. These snow boards are 30 cm $\times$ 30 cm with a 60 cm long measuring stick projecting from the center of the board. The Alta Avalanche Office visits the site at each time interval and records the height of snow measurements and uses a Snowmetrics snow density kit containing a spring scale, tube, and scraper to measure the density and weight of the newly fallen snow. The weight and density measurements acquired from these boards were used to validate those same measurements from the DEID. The site also has four automated snow measuring devices, including the NOAH II all weather precipitation gauge from ETI instruments and the Novalynx rain gauge. This instrument collects and records the weight of the newly fallen snow, and generates automated hourly SWE that is displayed on Mesowest (https://mesowest.utah.edu). Additionally, the site has three Campbell Sci. Inc. SR50 ultrasonic snow-depth sensors that record the height of snow and automatically upload the data to Mesowest every hour. These SR50 sensors also measure running totals on a 12 hr, total depth, and a storm frequency. Lastly, the site also has a live camera pointed at another 12 hr snowboard that is illuminated with lights for day or night 24 hr recording.

2.3.1 SNOWBOARD TILT TESTS

To better understand the relationship between the DEID's density profiles and new snow instability, we designed a repeatable shear-stability test based on standard tilt-board and shovel-tilt tests. A tilt-board stability test is a relatively easy method to quickly identify unstable layers in storm snow (Schweizer, Jamieson and Skjonsberg, 1998). The basic method was first developed over fifty years ago by V. Schleiss and W. Schleiss (1970) to investigate shear instabilities in new snow. As described by McClung, a tilt-board test makes use of an isolated 30 cm x 30 cm block of snow, no more than 40 cm deep that is placed on a metal plate. The plate is transferred to a horizontal board that pivots to 15 degrees. The plate is tapped when at 15 degrees until failure and the location of the failure plane is measured.

The standard field variant of the method, the *shovel tilt test*, isolates a approximately 30 cm x 30 cm column (again, no thicker than 40 cm) on a shovel which is tilted at 15 degrees and then tapped until shear occurs; tests are rated as Easy, Moderate, or Hard (Greene et al., 2004).

The tilt board used in our study, shown in Fig. 2.7, is a modified version of the standard method described

above. We purchased a snow board from Snowmetrics which is made of plastic and is 41 cm x 41 cm x 1.25 cm. Then we placed the snow board on an 80/20 T-slot aluminum frame that is affixed to the same crank-up mast that the DEID is mounted to. Our method was to have Alta Ski Patrol use this modified tilt board test every 12 hrs during their morning and afternoon observations at the Collins Study Plot.

Alta Ski Patrol was then asked to keep this snow board as close to the ground as possible to not have wind and other factors alter the natural snowfall. Each morning at approximately 04:00 LST Alta Ski Patrol would collect the data for us as follows: first, use your snow-saw to make the initial cut around the newly fallen snow, trying their best to not disturb the new snowfall. The cut is approximately the same dimensions as the snow board its self. After a cut was made, they would then use the hand crank on the mast to raise the snow and the board off the ground high enough to tilt the board to 30 degrees. Once the board was tilted to 30 degrees the snow practitioner would then place a finger on the top of the snow stake to be sure the sample was stable and would not fall off during the tilting step. Then they will begin the tapping process. 0-30 taps would then begin from the wrist and continue until there was a shear within the storm snow or no failure at 30 taps. If there was a shear, the practitioner would then record where the shear occurred and the number of taps required to produce the shear. If possible the grain type on the failure plane was recorded. We would repeat this process every 12 hrs with new snowfall at approximately 04:00 and 16:00 LST.

2.3.2 INFRASOUND AND UTAH AVALANCHE CENTER OBSERVATIONS

To aid in the validation of the new-snow instability model, data collected from the Infra-sound detection system is utilized (Vyas, 2009; Stephanie et al., 2020). The system is deployed through all prominent slide paths within LCC and detects the precise timing and location of avalanches by listening for the low frequencies generated by avalanches in motion on the north side of the road on SR-210. Once an avalanche is in motion the infra-sound systems detects the frequency and gives specific details about the avalanche, time in motion, power, and where it likely started and ended. To provide a larger picture of the avalanche activity in LCC and the surrounding region, observation data collected by the Utah Avalanche Center through a web portal submitted by recreationalists and snow professionals is used to assess the new-snow instability model.

CHAPTER 3

RESULTS

3.1 RESULTS RELATED TO OBJECTIVE 1: VALIDATION OF MEASURED PRIMARY VARIABLES

One of the most important purposes of the DEID is to provide accurate, real-time measurements of snow variables that are relevant to provide an understanding of storm-snow instability that are normally measured after the precipitation event. For example, variability in snow density and rapid changes in SWE can lead to an instabilities which can rapidly produce avalanches, but are often not identified until storm board, or snow pillow observations are collected and interpreted. Here we present several example results that illustrate the DEID's "real-time" capabilities. Figure 3.1 from 12 December 2020 shows a high-resolution density profile, SWE accumulation and rate against the standard weighing bucket (Figure 3.1b), and snow accumulation totals and rate against the standard ultra sonic snow height measurements (Figure 3.1c). The figure demonstrates that the DEID supplies far superior temporal resolution in the data, while agreeing with the collocated research grade instrumentation. For example at approximately 07:30 MST the SWE rate increased rapidly to 3.5 in hr^{-1} and then oscillates between 2 and 3 in hr^{-1} until just after 09:00 MST (Figure 3.1b). Over this same window in time the standard weighing bucket captures only three data points which miss/average out the rapid and important uptick of rapid SWE rate during this portion of the storm. In Figure 3.1c, the same features are observed for the snow rate and accumulation, which are critical parameters used for road clearing operations and chemicals use.

Figure 3.2 presents validation results from the DEID which demonstrate its ability to measure snow accumulation, SWE, and percent water with high accuracy. Data are collected from the seventeen different storms from the 2020-2021 season. For the validation data sets, 12-hr periods are used at the Alta Collins study plot, with manual measurements collected on a nearby snowboard. Superior agreement is found between the bulk standard measurement techniques and the summed DEID observations, with R^2 values of 0.994, 0.983, and 0.875 for SWE, snow accumulation, and snow density. It should be noted that further improvement of the bulk density measurements compared to the DEID totals may be improved with the inclusion of a densification model, since notable snow decomposition can occur within the 12 hours between manual observations. These key results provide a promising validation for the DEID, and mark the beginning of high resolution snow measurements. Future comparison studies where the DEID is placed in less-idealized study plots will be required to understand the DEID's fidelity in sampling areas where known under catch issues plague current technologies.

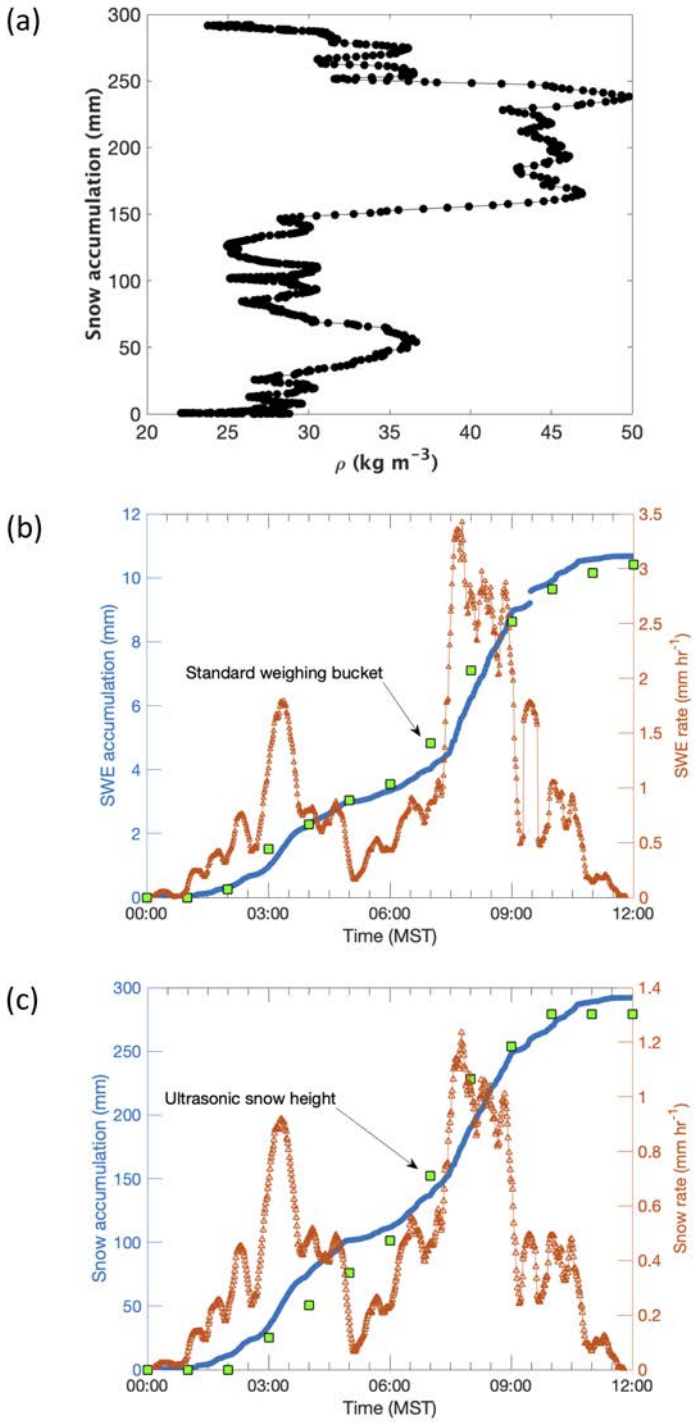

FIGURE 3.1

SWE and snow accumulation compared with a standard ETI bucket measurement and ultrasonic snow depth for one storm event on 12 December 2020. (a) Snow accumulation with density; (b)time series of SWE accumulation and SWE rate measured using the DEID and ETI gauge along with DEID-measured snow density. Each DEID data point represents a 1-min average and each ETI-gauge data point represents a 1-hours average. (c) Time series of snow accumulation and snow rate measured using the DEID and ultrasonic snow-depth sensor. Each DEID data point represents a 1-min average and Each ultrasonic data point represents a 1-hours average.

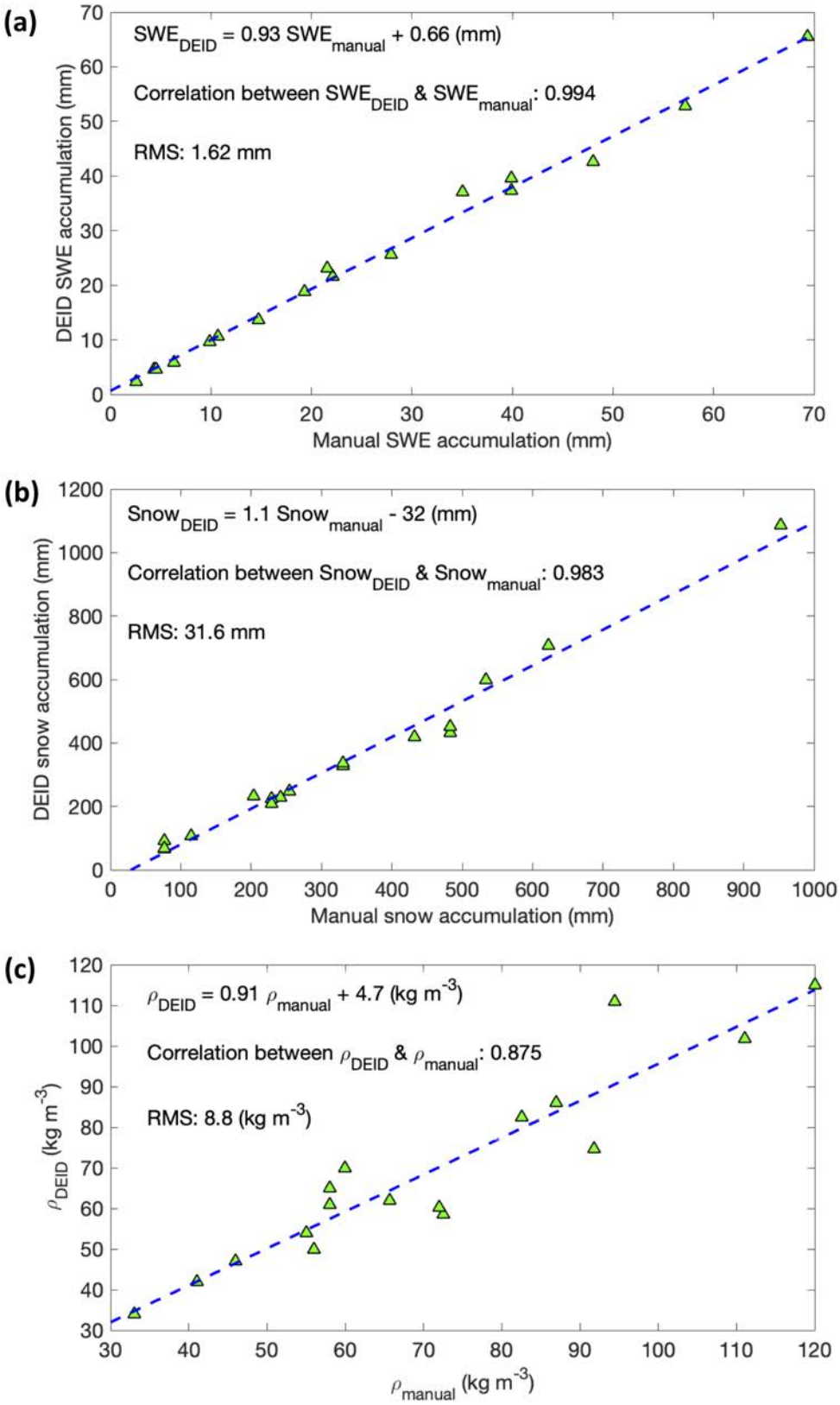

FIGURE 3.2

(a) SWE accumulation from DEID and manual measurements for seventeen storms. Each data point represents a storm. (b) Snow accumulation from DEID and manual measurements for seventeen storms. Manual measurements were made every 12 hours (04:00 and 16:00 LST), and the DEID sampled every second. (c) density of snow measured by DEID and manual measurement are compared for seventeen storms.

3.1.1 RESULTS FOR OBJECTIVE 2: STABILITY RESULTS

Results are presented from the DEID from during the 2020-2021 winter season. Over the course of the season, the DEID captured data from each storm. For this report, data from nine storms from 12 December 2020 to 22 March 2021 are analyzed and presented. To understand the conditions and avalanche hazards after each storm, data collected from the DEID, the infrasound detection system, and physical observations from the Utah Avalanche Center were combined to paint a complete picture of the avalanche activity and storm-snow stability. A summary of these results can be found in Table 3.1. Table 3.1 provides details on the storm start time, end time, total snow accumulation, total SWE, max SWE rate, mean storm-snow density, maximum density gradient in the storm snow, and the ensemble averaged stability index from the four models. It should be noted that all of these variables are measured directly or derived solely from DEID observations. The columns that follow the DEID-derived data provide insight into the avalanche conditions in the Central Wasatch through information from tilt-board test results at the mid-Collins site, time of first infrasound avalanche detected in LCC, and post 3-day totals of avalanches observed in the Central Wasatch.

Of the nine storms captured and reported in Table 3.1, three storms from the 2020–2021 season were identified for their storm characteristics and forecasted "new-snow" avalanche problem as noted by the Utah Avalanche Center (UAC) and post-storm activity. These storms are as follows:

1. **12 December 2020**: Avalanche observations show one positive natural occurred in the new snow and three user-triggered avalanches occurred; the forecast demonstrated that the new snow was sensitive to skier-triggering following the storm through photos and videos. Report details can be found here: 12/13/2020 UAC Forecast
2. **27 February 2021**: Report details can be found here: 2/27/2021 UAC Forecast
3. **20 March 2021**: Two reported natural avalanches and four reported skier-triggered avalanches that were 8-12 inches deep and failing in the new snow. A key observation can be found here: 3/20/2021 Key Observation and report details can be found here: 3/20/2021 UAC Forecast

To better understand the DEID-based instability model presented in Section 2.2, detailed results from the model are supplied in Figs. 3.3 through 3.8. These results are solely produced by the DEID and highlight the input, derived, and final variables (outputs) for each of our three case studies described above. Figures 3.3, 3.5, and 3.7 provide model results for the model run with coefficients derived from Jamieson and Johnston (2001) coupled with the Conway and Wilbour (1999) compression model. Other model member results are not shown since they show similar trends for each case. For each case subplot, (a) presents the density of the snowfall during the storm (solid line) and the density of the storm snow at the end of storm with the densification model. Subplot (b) is the storm-snow density with densification over the time of the storm, which is used to compute the storm-snow strength over time (c) and overburden (d). Lastly, subplots (e) and (f) present the stability index (SI), which is the ratio of subplot (d) to (c), and the time to failure, computed following the method of Conway and Wilbour (1999).

Figures 3.4, 3.6, and 3.8 provides the stability index and time to failure for the basal layer of the snow pack using the four models presented in Table 2.1 and an ensemble of all models to begin to provide a statistical avalanche forecasting tool. This approach is akin to the weather forecasting approach where multiple models with a variety of initial conditions are supplied to understand the ensemble of all models as well as the convergence of those models. It should also be notes that this figure can be produced for any storm layer of interest, but the basal is studied for simple interpretation of the results.

Details from the storm on 12 December are supplied in Figs. 3.3 and 3.4. Initial density profiles from the

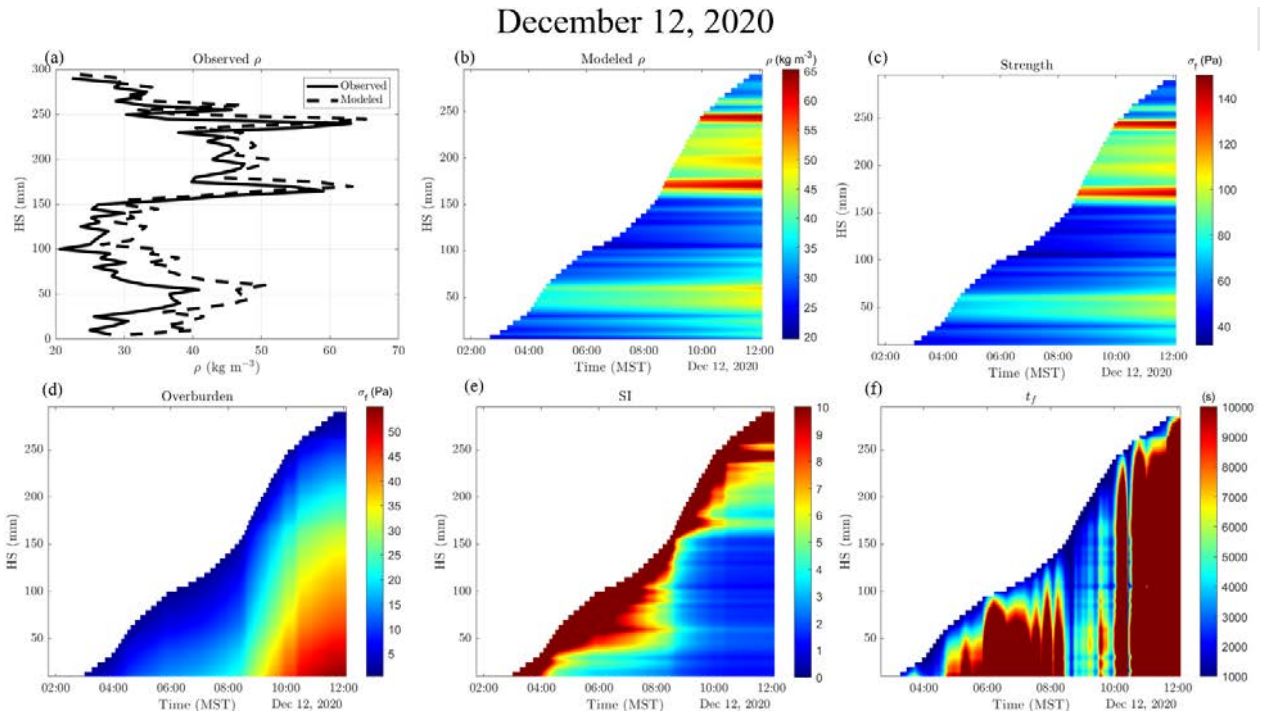

FIGURE 3.3

Avalanche forecasting plots produced with data from the DEID for storm beginning on 12, December 2020. (a) The measured and modeled density profile of the storm snow, (b) The modeled storm snow density over the course of the storm, (c) the modeled shear strength of the storm snow, (d) the measured overburden force of the storm snow, (e) the stability index (ratio of subplot c to subplot d), and (f) the predicted time to failure in seconds of the storm snow.

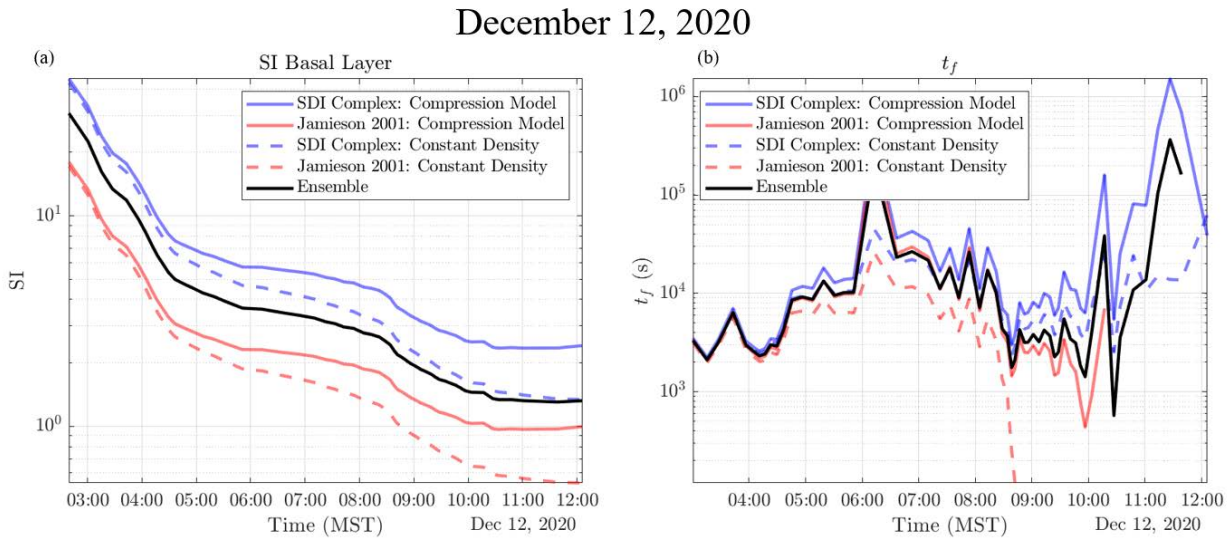

FIGURE 3.4

Basal layer plots of (a) stability index (SI) and (b) the time to failure for storm snow data beginning on 12 December 2020.

storm snow (Fig. 3.3 a and b) show low density (20–30 kg m^3) snow in the lower 150 mm with higher density snow (60 kg m^3) above these layers at 50 mm and from 150 mm to 200 mm. This high level of detail in the storm-snow density indicates the existence of slight density inversions, which are present in the strength profile (Fig. 3.3 c). Here, blue indicates weaker snow, as seen at the basal layer, and red indicates stronger snow. Figure 3.3 e presents the SI, which indicates fragile storm snow, as indicated by the appearance of the blue region at the storms end from the basal layer to 150 mm. This is further substantiated in the time to failure (Fig. 3.3 f) with the striking blue vertical lines indicating 1000 seconds to failure at 10:40 on 12 December 2020, as well as Figs. 3.4 a and b. From this analysis, we find that this model did predict the onset of naturals, however our ensemble of models (black line in Figure 3.4 b) did not, but came very close (minimum SI of 1.29). This result is indicative of a very sensitive snowpack and is further seen in the results in Table 3.1, showing five reported avalanches with one natural from observations in the region.

Findings from 26 February 2021 present another case with a new-snow avalanche problem which produced a sensitive snow pack with a limited number of naturals (Figs. 3.5 and 3.6). The initial density profile (Fig. 3.5 a) from the storm does indicates a slight inversion, however, the low stability index near the surface is in part driven by the large overloading from the high precipitation rates observed over the course of the storm, tipping the scales toward instability. This can be observed in Fig. 3.5 f, which presents the time to failure model. Here, areas of red indicate strengthening, with vertical lines of light color being associated with moments of high precipitation and increasing danger. These periods are identified at approximately 08:00 on 27 February 2021 and at noon on the same day, both correlating with a small natural cycle which was captured by the infrasound detection system (Table 3.1).

A similar storm was captured on 20 March 2021 (Figs. 3.7 and 3.8), however this storm provided interesting results which capture a right-side up snowpack in the lower 200 mm, with a strong density inversion from 200–350 mm. These layers from 200–350 mm within the storm snow provided the problematic layer for which 8 reported avalanches failed on in the Central Wasatch (see provided observations in the storm details list at the beginning of the section). Not only did the models capture this slight variation within the storm snow, the SDI Complexity without compression and the Jamieson and Johnston (2001) with compression both correctly predict the onset of naturals within the problematic layers. However as explored in the following Section a wide variation of the models existed for this storm.

3.1.2 RESULTS FOR OBJECTIVE 2: TILT-BOARD TEST RESULTS

DEID data from the 5 February 2021 storm was captured and compared to Alta Ski Patrol's manual observations and tilt-board tests. Figure 3.9 presents a schematic of the tilt-board test results (a) and profiles of the storm-snow density (b), SDI (c), $Complexity$ (d), SWE rate (e), and modeled shear strength (f) from the SNOSS model with strength coefficients SDI and $Complexity$ without densification. In each profile, the red line represents the weak layer/failure plane within the storm snow that failed during the tilt-board test.

Figure 3.9a is a schematic of the tilt-board test results. For this test, 12-hrs of storm snow accumulated onto the board. During the test, the board was raised from the snow surface, tilted to 30 degrees and tapped following the procedure in Section 2.3.1. A shear failure occurred at a height of 152 mm from the boards surface after the fourth tap. To understand this result, we provide a detailed account of the variables measured by the DEID.

Over the course of the entire study period, the macro trend in density tended to increase throughout the entire storm (Fig. 3.9b). However, due to the detail captured by the DEID, we are able to observe the local minima in density, with specific attention to the local minimum at the weak layer (HS= 152 mm, ρ = 70 kg m^3),

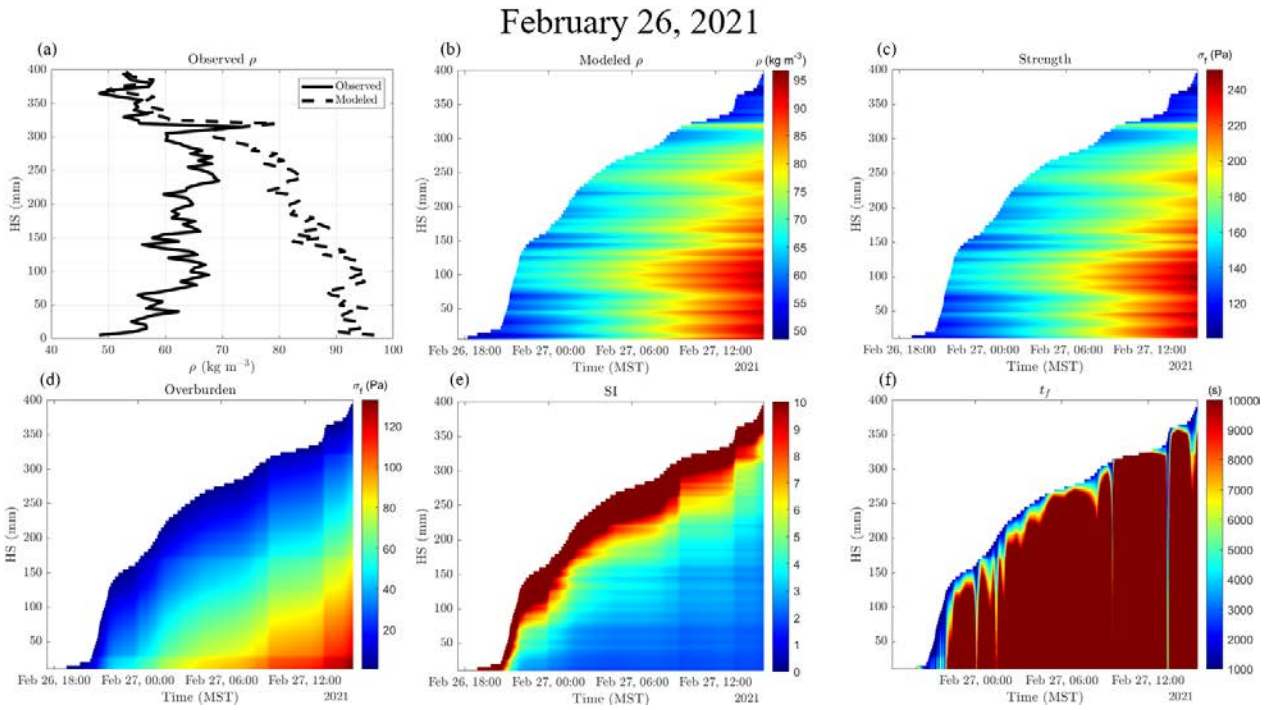

FIGURE 3.5

Avalanche forecasting plots produced with data from the DEID for storm beginning on 26, February 2021. (a) The measured and modeled density profile of the storm snow, (b) The modeled storm snow density over the course of the storm, (c) the modeled shear strength of the storm snow, (d) the measured overburden force of the storm snow, (e) the stability index (ratio of subplot c to subplot d), and (f) the predicted time to failure in seconds of the storm snow.

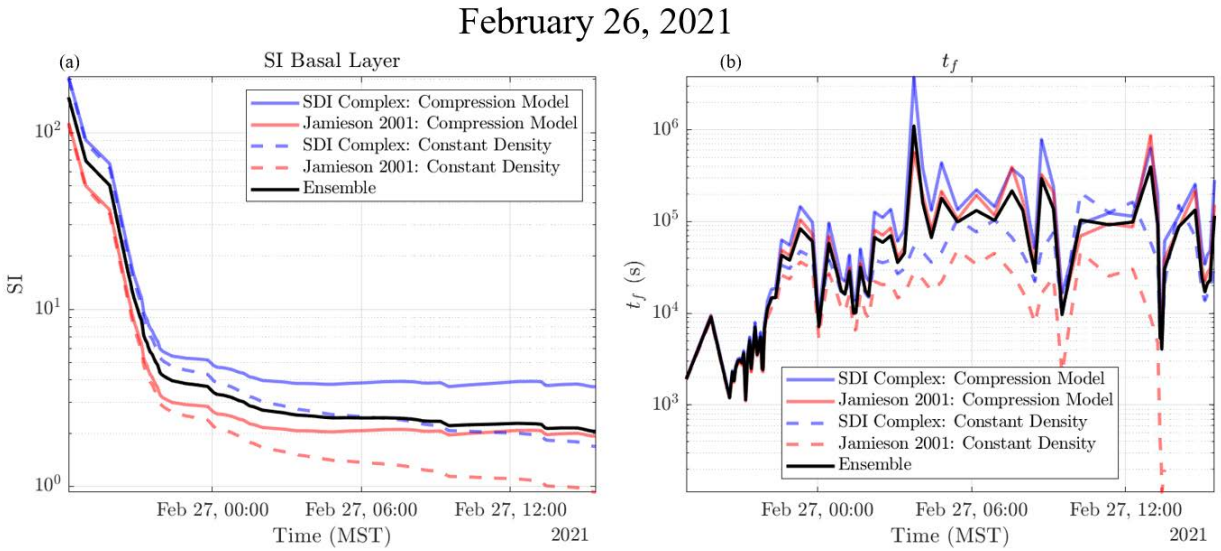

FIGURE 3.6

Basal layer plots of (a) stability index (SI) and (b) the time to failure for storm snow data beginning on 26 February 2021.

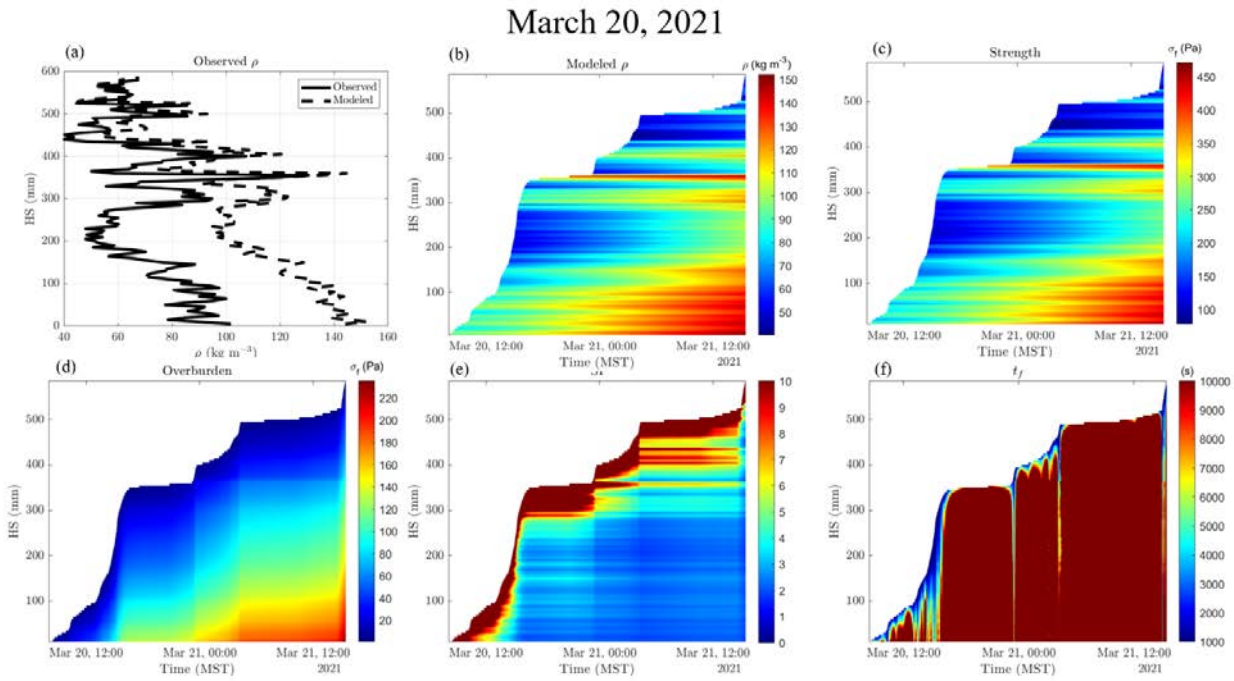

FIGURE 3.7

Avalanche forecasting plots produced with data from the DEID for storm beginning on 12, December 2020. (a) The measured and modeled density profile of the storm snow, (b) The modeled storm snow density over the course of the storm, (c) the modeled shear strength of the storm snow, (d) the measured overburden force of the storm snow, (e) the stability index (ratio of subplot c to subplot d), and (f) the predicted time to failure in seconds of the storm snow.

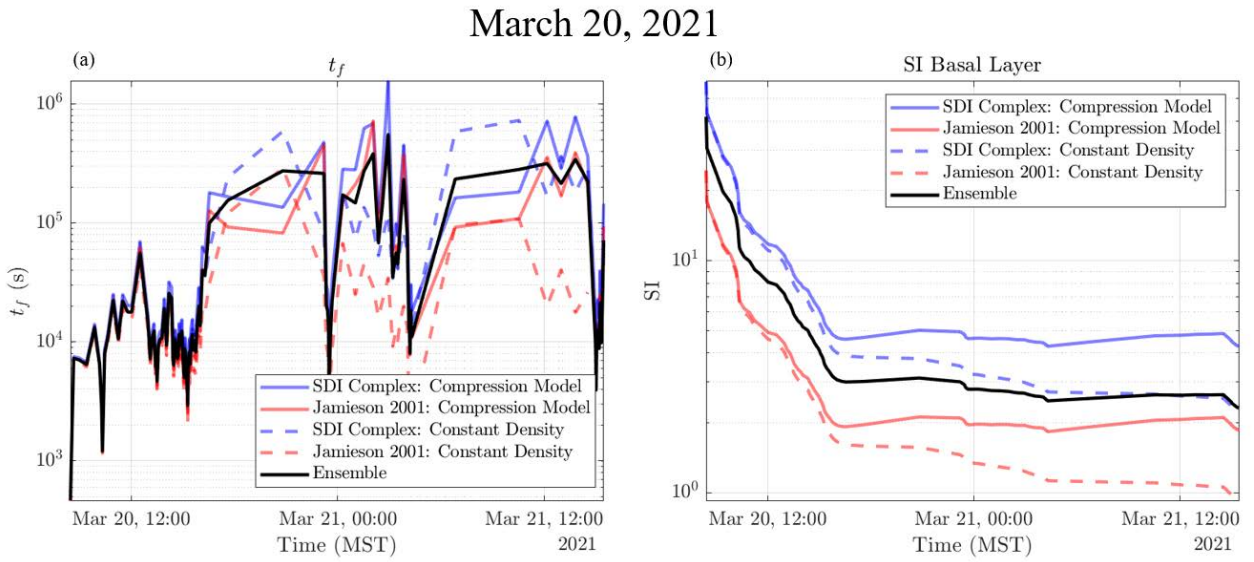

FIGURE 3.8
Basal layer plots of (a) stability index (SI) and (b) the time to failure for storm snow data beginning on 20 March 2021.

followed by a local maximum in density at 200 mm (HS= 190 mm, ρ = 118 kg m^3). This detail is important and interesting since the macro trends (which would only be captured by traditional methods) would observe this density profile and conclude that the weakest layer is the global minimum (HS= 10 mm, ρ = 45 kg m^3). However, since shear strength of snow is a function of density and snowflake habit, this conclusion, which only examines density, would misidentify the weakest layer in the new snow.

Specifically, Fig. 3.9c shows a profile of snowflake SDI. Snowflake SDI is observed to decrease throughout the storm cycle to its minimum at the weak layer snow height, from a value of 9 to 5 (reduction in 44 percent). Meanwhile, Fig. 3.9d presents the snowflake $Complexity$, which was found to increase from approximately 1.32 to 1.45 at the shear layer (global maximum). From Section 2.2.2, this trend and combination of SDI and $Complexity$ indicate that the snowflake habit changed during this period to a planar-crystal habit. Figure 3.9e provides a detailed look at the SWE rate as a function of snow height with a notable peak in SWE rate at the height of the weak layer.

From this information, we can estimate the snow's shear strength and conclude that the layer at 152 mm is the weakest layer by utilizing the shear-strength model, which accounts for SDI and $Complexity$ without densification (Fig. 3.9f). Here, the global minimum in shear strength is correctly identified by the DEID and correlates with results from the manually observed tilt-board test. This result presents the power of the DEID to not only capture density profiles in great detail but to aid in determining storm-snow instabilities, which may require information about snowflake habit and natural avalanches. These results provide an example of how real-time output from the DEID can be used by snow practitioners to make real-time forecasting decisions.

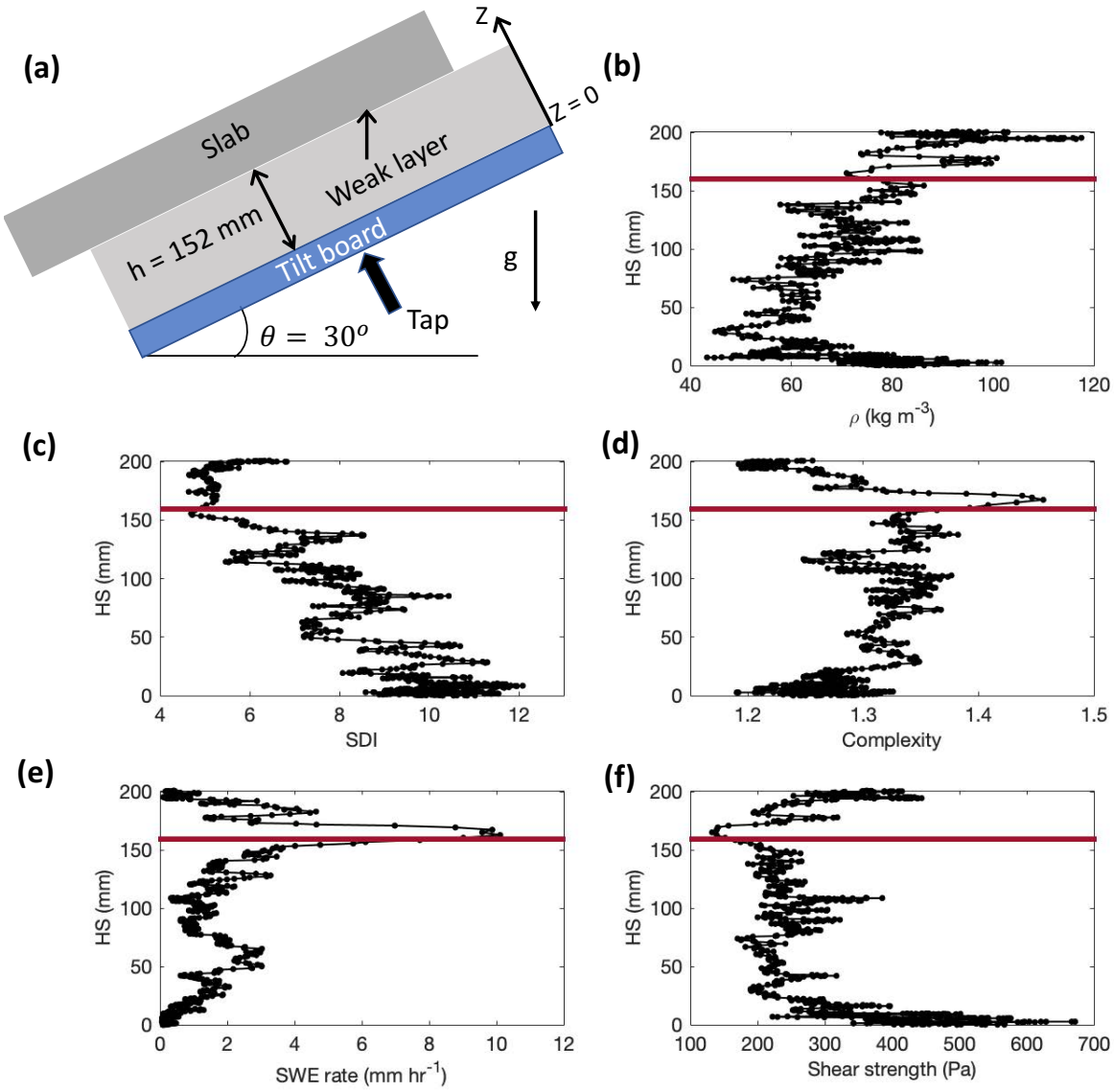

FIGURE 3.9

DEID data from a snow event on 5 Feb 2021 that corresponds to a tilt-board test in which the snowpack failed at 152 mm from base (z = 0) in 4 taps. (a) Schematic of tilt-test set-up; (b) height of snow vs. density; (c) height of snow vs. SDI; (d) height of snow vs. $Complexity$; (e) height of snow vs. SWE rate (f) Height of snow vs. shear strength.

New Snow Stability Metrics										
Storm Start Time/Day (MST)	Storm End Time/Day (MST)	total Snow (mm)	total SWE (mm)	max SWE rate (mm/h)	$\overline{\rho}$ (kg/m^3)	$\frac{\delta\rho}{\delta z}\|_{max}$ (kg/m^4)	SI_{min}	Tilt Board Test	Infrasound	UAC Observed Avalanches
0100 12/12	2000 12/12	292	10.66	5.16	34	17	1.30	NA	NEG	5 (1/3/**1**/0)
0600 12/17	0700 12/18	413	27	11.24	63	200	1.22	NA	POS: 0025 12/18	41 (7/16/**18**/0)
0900 12/22	0900 12/23	314	15.38	31	54	12	1.14	NA	NEG	11 (5/4/**2**/0)
0845 01/22	0600 01/24	457	34.37	50	71	- 29	0.96	NA	NEG	27 (5/12/**10**/0)
0600 02/03	2000 02/05	488	31.75	28.93	70	200	1.29	POS	POS: 1515 02/05	34 (4/6/**24**/0)
2125 02/11	1600 02/14	862	51.81	8.91	57	56	0.91	POS	POS: 0244 02/12	155 (10/5/**72**/69)
0000 02/15	2000 02/17	1078	65.15	29	57	178	0.47	NA	POS: 0058 02/16	114 (4/1/**55**/54)
1611 02/26	1600 02/27	402	24.13	13.01	59	76	1.50	NA	POS: 0730 02/27	12 (2/5/**5**/0)
0743 03/20	2000 03/22	598	33.35	9.11	50	22	1.39	POS	POS: 0735 03/21	8 (2/4/**2**/0)
0715 03/25	0600 03/26	323	16.79	24.02	54	53	3.79	NA	NEG: 0735 03/21	10 (1/4/**5**/0)
0433 04/26	1300 04/26	272	35	11.4	83	- 180	1.43	NA	NEG: 0735 03/21	7 (2/4/**1**/0)

TABLE 3.1

Table of DEID measured parameters and snow stability metrics during winter 2020-2021 for ten different snow events observed in Little Cottonwood Canyon. Tilt board test are "POS" or "NEG" for positive or negative results, and if a positive result occurs, the number of taps are shown. Infrasound - indicates if infrasound results were positive and when. UAC observations indicate the total number of avalanches reported during that period and the number of trigger types in the format unknown/user/natural/explosive. Natural avalanches are in boldface type. NA indicates data “not available”

CHAPTER 4

DISCUSSION

Within the strength to overburden model a high level of sensitivity exists on the coefficients of strength used in Eq. 2.7 (i.e., λ and β). At current, these strength coefficients are only a function of the simple grain type (i.e. facets, precipitation particles, etc.). Here, we present and asses a model which accounts for the shape and complexity of precipitation (SDI and complexity model), which relates to the precipitation classification as shown in Section 2.2.2. While this model requires further validation, this method accounts for the variety of strength different precipitation particles may have based on their complex structure. For example, it is known from expert experience that all snow flake habits (dendrites, columns, and graupel) exhibit different shear strengths. Despite this, precipitation particles in all new snow stability models are assumed to have the same shear strength coefficients. This is not due to that lack of understanding of the importance of snow flake habit on shear strength, rather the difficulty to measure real-time snow flake habit, then measure the respective shear strength immediately after snowfall. Therefore it is left to the density of the particle to determine its shear strength (Eq. 2.7). To assess this newly proposed SDI and $Complexity$ model in the context of the existing models, four strength models, as described in Section 2.2, as well as the ensemble of all models, are utilized to statistically predict the onset of new snow avalanches. The four models and a summary of their performance are summarized in Table 4.1.

Of the four models, we found that the ensemble, Jamieson and Johnston (2001) with compression, and the SDI and $Complexity$ model without compression provided the best predictions of the onset of naturals. Although, as discussed below, by collecting data from the model and the natural avalanche activity a specific SI may be used to further understand each model. In other words, Jamieson and Johnston (2001) without compression may have a critical SI value of 0.5 and the SDI and $Complexity$ model with compression

Model	Tendency	Explanation
Jamieson 2001, no compression model	Conservative	Lowest coefficients of strength, with constant density
Jamieson 2001, with compression model	Fair	Lowest coefficients of strength, with increasing density
SDI & Complexity, no compression model	Fair	Larger coefficients of strength, with constant density
SDI & Complexity, with compression model	Liberal	Larger coefficients of strength, with increasing density
Ensemble	Fair	Average of all models

TABLE 4.1
A summary of the shear-strength model evaluations. Jamieson 2001 is an abbreviation for Jamieson and Johnston (2001)

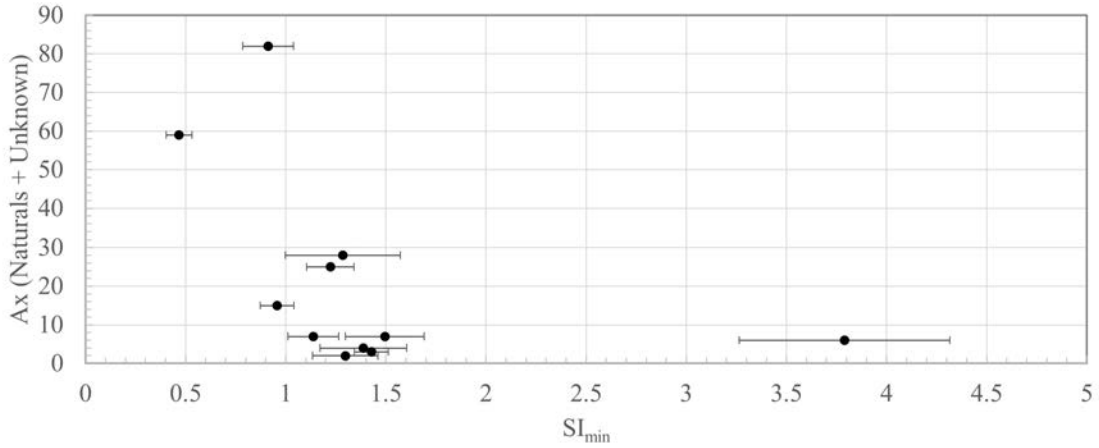

FIGURE 4.1
The total number of natural and unknown triggered avalanches reported to the Utah Avalanche Center from storm's end to three day post storm, compared to the ensemble averaged stability index. The error bars represent the standard deviation between the models for each case. When fit with a power law function, a best fit of $Ax = 15.2SI_{min}^{-1.4}$ is found with an $R^2 = 0.4$

may have a critical SI of 3. The reason behind this variability lies within the coefficients of strength and the compression model parameters. Further research, which can now be performed with instruments like the DEID, MASC, and strain gauges can help us begin to define specific strength coefficients for grain types. Furthermore, with the availability of more storms and data, we can begin to further validate Table 2.2 such that these classifications and strength predictions can be performed with the DEID solely.

As mentioned above, one of the critical differences between the models is the inclusion (or exclusion) of the density compression model (i.e., densification). The goal of the model is to account for the compression the snow experiences due to metamorphic and vertical overburden stresses over the lifetime of the storm to provide a more realistic density profile. The model treats the snow as a fluid which compresses (reduces volume) based on the inherit compressive viscosity of the snow. Initial observations from model runs suggest that the model may be compressing the snow pack more rapidly than anticipated. We hypothesize that the reason for this discrepancy is the original density, strength, and viscosity parameters are all measured in a "post storm " fashion. Traditional methods for capturing these parameters requires digging snow pits, hours or even days after the storm snow has settled, compressed, and begin to under go metamorphism. Moreover, as with the original strength coefficients, the compactive viscosity is only a function of crystal type, not precipitation type. Casson, Stoelinga and Locatelli (2008) performed a study to further begin to classify the compressive viscosity as a function of precipitation type, however, no clear conclusions were drawn. With the new high resolution data from the DEID we are examining timescales which may require new studies to reveal the compactive viscosity over short time scales and for specific precipitation particle types. Going forward, discovery of the compressive viscosity terms as a function of crystal type and shorter timescales may being to improve the storm snow density compression model and improve avalanche forecasting.

The stability index (SI), Eq. 2.11, represents the ratio of the overburden stress to the shear strength of the storm snow. Physically, it is understood that when the SI falls below unity, the snowpack is unstable and natural avalanches may be begin to occur. However, this may not be the correct indicator for when naturals begin to occur due to terrain, variability in snow accumulation, and differences in elevation. While the point

assessment of the stability model has its complexities, we attempt an initial statistical study of the correlation between the minimum stability index (SI_{min}) and number of reported avalanches. This may help place more context on the value of the SI as well as the convergence of the models used to asses the SI. Figure 4.1 shows this correlation by plotting calculated ensemble SI_{min} against the number reported avalanches occurring in the Central Wasatch from the storms end to three days post storm. Initial findings suggest that the number of reported avalanches is a function of the SI_{min}. This suggests that as more data are collected, the sensitivity and precise number of avalanches expected from any one storm can be estimated with the SI model for a particular region. Further studies designed to collect more data may be able to unlock more insight into the physical meaning of the spectrum of stability indices each model presents. We hypothesize that other data may be used to adapt this for applicability to regions outside of Little Cottonwood Canyon.

CHAPTER 5

CONCLUSION

Results are presented which highlight the Differential Emissivity Imaging Disdrometer's ability to obtain real-time measurements of critical meteorological variables for avalanche forecasting and snow observations. Accurate measurements of snow density, snow water equivalent, and snow accumulation are all provided in a particle by particle fashion with results here shown at 5 mm resolution. These parameters are critical in nowcasting avalanche hazard and have never been available at such high resolution. Furthermore, newly developed parameters, which are captured from the DEID include the snow density index (SDI), which is the ratio of the actual projected snowflake area measured on the DEID's hotplate to the melted area of the snowflake, and the snowflake's $Complexity$, or the ratio of the area of the smallest ellipse altogether containing the particle cross-section to the actual cross-sectional area of the hydrometeor. Classification of snowflake habit based on these parameters are presented in Section 2.2.2. In conjunction with the overlaying SWE measurements from a storm, or overburden stress, the stability index of the new snow and time to failure metrics are computed for four different models.

5.1 CHALLENGES AND FUTURE WORK

Remaining challenges regarding the DEID system exist and provide the platform for future research and development. The following is a list covering the most current and urgent areas of future work.

- Loss of data due to power loss is always an issue for remote weather observations systems, and the DEID is no exception. To combat this, the DEID was deployed with an interrupted power supply (UPS) during the 21-22 winter season and to date no data loss has occurred due to loss of power.
- Currently this system is semi-autonomous and requires consistent data handling and manual processing of data. We are working on automating this process and analyzing the data real-time, allowing for updated data and plots every 5-15 minutes.
- An automated and optimized way to maintain the hotplate temperature at a fixed ΔT above ambient would improve reliability of results. Current methods monitor the plate temperature and will require refinement for harsher environments.
- Automation of the cleaning of the plate will help mitigate the impact of impurities which land on the plate. This is currently managed by allow this first millimeters of a storm to accumulate on the

plate, then powering it, letting the fresh melt run the impurities off the plate. Other impurities must be mechanically removed from the hotplate surface.

- During periods of high SWE, snowflake overlap may be observed. Despite this impacting the DEID's ability to measure SDI, $Complexity$ and density, it does not effect SWE or snow depth quantification. Future improvements may increase the hotplate temperature momentary during these extreme and rare events to reduce evaporation times (although reductions are limited by the Leidenfrost effect).

5.2 SIGNIFICANT RESULTS AND POTENTIAL IMPACTS

Key areas from the project that may result in significant increases in reliability of the DEID outputs as well as improvements that will increase the DEIDs impact on society are provided below.

- Providing and validating measurements of the liquid water content (the amount of liquid water in a volume of space). This variable is important due to its widespread use in forecasting tools, thus providing a straightforward variable for down scaling. Initial results of this work can be observed in Fig. 5.2.
- Given the DEID's ability to estimate the shear layer within a new-snow instability and measure overburden weight, the rupture size of a new-snow avalanche can be estimated using the DEID. The rupture size could then be estimated for relevant slide paths of interest and relate this to the D-scale. For further details see V. Schleiss and W. Schleiss (1970).
- We have found that the parameterization of the compression viscosity in the SNOSS model may be too aggressive (producing snow that is too strong) for our rapid and highly detailed data from the DEID. We hypothesize that improvements of this model can be made through performing field and lab experiments to refine these parameters for crystal structure and over shorter periods of time.
- One of the key findings we present is the DEID's ability to classify snowflake habit from SDI and $Complexity$. We wish to further validate and improve the snowflake habit identification technique from the DEID for both new and old snow-crystal structures.
- Optical visibility degradation during precipitation can be estimated from the DEID (Fig. 5.1). Methods and results of this approach can be found in Singh et al. (2021). Further validation with standard visibility sensors and optical imagery are required. For example, the forward scattering present weather detector (Oppermann and Williams, 2018).
- The DEID is capable of identifying different snow-crystal types using SDI and $Complexity$. What is not well understood is how mixtures of different snow-crystal types impact the strength of different layers. Currently, our stability index model simply linearly averages all types of snow crystals contained in a 5-mm layer, but it is not clear if this is the correct way to combine them to best model snow strength. Future work should investigate the relationship between snow-crystal type and shear strength using the DEID to differentiate particle types.

5.3 PROSPECTUS

Here, we have explored a promising, yet simple stability index model that makes use of the DEID's unique and highly detailed dataset in near real-time. Future work and studies should expand the modeling approaches

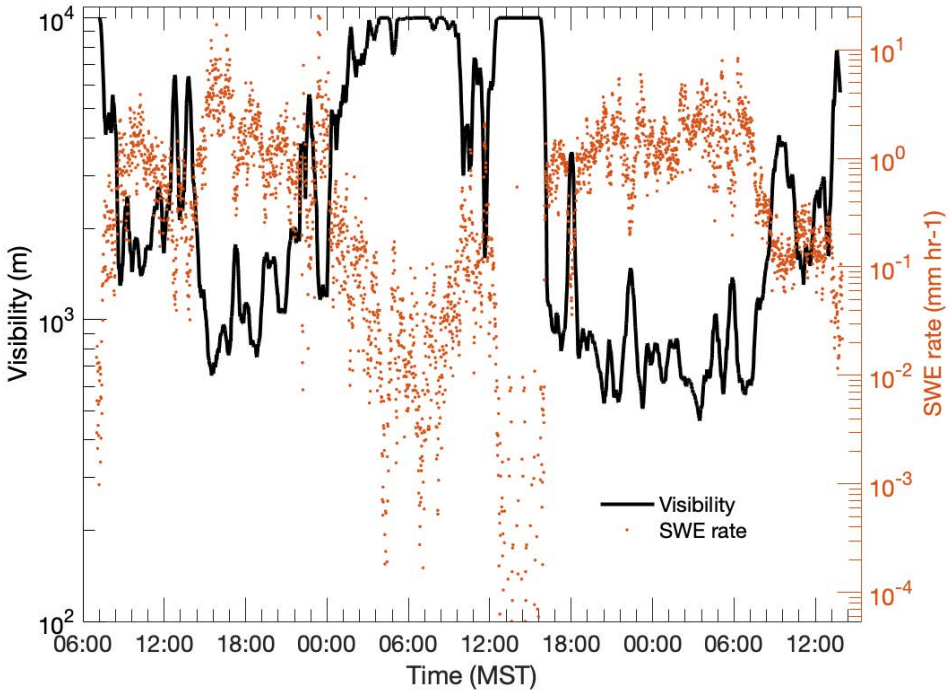

FIGURE 5.1
Time series of 1-minutes averaged visibility and SWE rate using DEID data. The data are from 11 Feb to 14 Feb 2021.

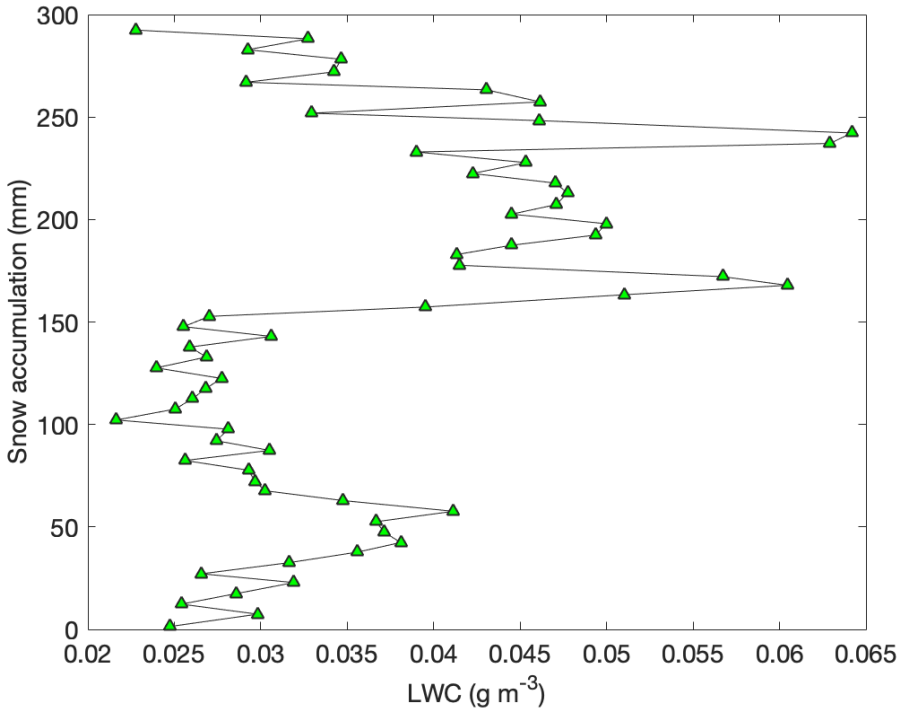

FIGURE 5.2
Liquid water content (LWC) in a snow pack. LWC is estimated in each 5 mm snow layer. The data are from 12 Dec 2020 storm.

to include more sophisticated, physics-based avalanche modeling tools (*e.g.* SNOWPACK or CROCUS). Combining advanced avalanche modeling tools with the DEID and diagnostics like the Infrasound Detection Systems will provide the ingredients to significantly advance the state of science for avalanche forecasting. Finally, the knowledge gained from this work is being used by Particle Flux Analytics, Inc. to develop and commercialize an instrument and software that can purchased by TARP and other avalanche professionals.

BIBLIOGRAPHY

Singh, D. K. et al. (2021). 'A differential emissivity imaging technique for measuring hydrometeor mass and type'. In: *Atmospheric Measurement Techniques* 14(11), pp. 6973–6990. DOI: 10.5194/amt-14-6973-2021. URL: https://amt.copernicus.org/articles/14/6973/2021/.

Vyas, M. (2009). *Infrasound avalanche monitoring system research evaluation*. Utah Department of Transportation.

Stephanie, M. et al. (2020). 'Evaluating the performance of an operational infrasound avalanche detection system at three locations in the Swiss Alps during two winter seasons'. In: *Cold Regions Science and Technology* 173, p. 102962. ISSN: 0165-232X. DOI: https://doi.org/10.1016/j.coldregions.2019.102962. URL: https://www.sciencedirect.com/science/article/pii/S0165232X19302332.

Nalli, W. (2019). personal communication.

Rees, K. N. et al. (2021). 'Mass and density of individual frozen hydrometeors'. In: *Atmospheric Chemistry and Physics* 21(18), pp. 14235–14250.

Gultepe, I. and J. Milbrandt (2010). 'Probabilistic parameterizations of visibility using observations of rain precipitation rate, relative humidity, and visibility'. In: *J. Appl. Meteor. Climatol.* 49, pp. 36–46.

Rasmussen, Roy M. et al. (1999). 'The estimation of snowfall rate using visibility'. In: *J. Appl. Meteorol.* 38, pp. 1542–1563.

Hayes, P. et al. (2004). 'A simple model of snow slope stability during storms'. In: *Proceedings of the 2004 International Snow Science Workshop, Jackson Hole, WY*, pp. 165–171.

Conway, H. and C. Wilbour (1999). 'Evolution of snow slope stability during storms'. In: *Cold Regions Science and Technology* 30, pp. 67–77.

Havens, S. et al. (2012). 'Real time snow slope stability modeling of direct action avalanches'. In: *Proceedings of the 2012 International Snow Science Workshop, Anchorage, Alaska*, pp. 866–871.

Jamieson, J. B. and C. D. Johnston (2001). 'Evaluation of the shear frame test for weak snowpack layers'. In: *Annals of Glaciology* 32, pp. 59–69. ISSN: 0260-3055. DOI: 10.3189/172756401781819472.

Perla, R., T. M. H. Beck and T. T. Cheng (1982). 'The shear strength index of alpine snow'. In: *Cold Regions Science and Technology* 6, pp. 11–20. DOI: 10.1016/0165-232x(82)90040-4.

Jamieson, J. B. (1995). *Avalanche prediction for persistent snow slabs*. DOI: 10.11575/PRISM/10182. URL: https://prism.ucalgary.ca/handle/1880/29827.

Kojima, K. (1967). 'Densification of Seasonal Snow Cover'. In: *Physics of Ice and Snow: Proceed. Int. Conf. on Low Temperature Science*. Physics of Snow and Ice: Proc. Int. Conf. on Low Temperature Science. Institute of Low Temperature Science: Sapporo, Japan, pp. 929–952.

Fierz, CRLA et al. (2009). 'The international classification for seasonal snow on the ground'. In.

Praz, Christophe, Yves-Alain Roulet and Alexis Berne (2017). 'Solid hydrometeor classification and riming degree estimation from pictures collected with a Multi-Angle Snowflake Camera'. In: *Atmospheric Measurement Techniques* 10(4), pp. 1335–1357.

Garrett, T. J. et al. (2012). 'Fall speed measurement and high-resolution multi-angle photography of hydrometeors in free fall'. In: *Atmospheric Measurement Techniques* 5(11), pp. 2625–2633. DOI: 10.5194/amt-5-2625-2012.

Schweizer, J., S. Bellaire et al. (2006). 'Evaluating and improving the stability predictions of the snow cover model SNOWPACK'. In: *Cold Regions Science and Technology* 46(1), pp. 52–59.

Casson, J., M. Stoelinga and J. Locatelli (2008). 'Evaluating the importance of crystal-type on new snow instability: a strength vs. stress approach using the SNOSS model'. In: *Proceedings of the 2008 International Snow Science Workshop, Whistler, BC*, pp. 612–619.

Brun, E. and L. Rey (1987). 'Field study on snow mechanical properties with special regard to liquid water content'. In: *IAHS Publ* 162, pp. 183–193.

Schweizer, J., J. B. Jamieson and D. Skjonsberg (1998). 'Avalanche forecasting for transportation corridor and backcountry in Glacier National Park (BC, Canada)'. In: *Proceedings of the Anniversary Conference*. Vol. 25, pp. 238–244.

Schleiss, V. and W. Schleiss (1970). 'Avalanche hazard evaluation and forecast, Roger Pass, Glacier National Park. In Ice engineering and avalanche forecasting and control'. In: *Technical Memorandum 98, Natl. Res. Counc. Can.*, pp. 115–122.

Greene, E. et al. (2004). 'Snow, weather, and avalanches: Observational guidelines for avalanche programs in the United States'. In: *American Avalanche Association, Pagosa Springs, Colorado* 150.

Oppermann, Cody and Jeff Williams (2018). 'The Utah Department of Transportation's Winter Road Weather Index, Storm Intensity Index, and Snow and Ice Performance Measure'. In: *Utah Department of Transportation*.